Helmholtz-Zentrum Dresden-Rossendorf (HZDR)

Hydrodynamics, mixing and mass transfer in a pilot-scale bubble column with dense internals

Möller, F.; Lavetty, C.; Schleicher, E.; Löschau, M.; Hampel, U.; Schubert, M.;

Originally published:

March 2019

Chemical Engineering Science 202(2019), 491-507

DOI: https://doi.org/10.1016/j.ces.2019.03.001

Perma-Link to Publication Repository of HZDR:

https://www.hzdr.de/publications/Publ-28312

Release of the secondary publication
on the basis of the German Copyright Law § 38 Section 4.

CC BY-NC-ND

*Manuscript
Click here to view linked References

Hydrodynamics, mixing and mass transfer in a pilot-scale bubble column with dense internals

Felix Möller[1,*], *Craig Lavetty*[1], *Eckhard Schleicher*[1], *Martin Löschau*[2], *Uwe Hampel*[1, 3], *Markus Schubert*[1]

[1]Institute of Fluid Dynamics, Helmholtz-Zentrum Dresden-Rossendorf, Bautzner Landstr. 400, 01328 Dresden, Germany

[2]Teletronic Rossendorf GmbH, Bautzner Landstr. 45, 01454 Großerkmannsdorf

[3]Chair of Imaging Techniques in Energy and Process Engineering, Technische Universität Dresden, 01062 Dresden, Germany

[*]Corresponding author

Abstract

Bubble column reactors with exothermic reactions are often equipped with dense tube bundle heat exchangers. While there is some knowledge about the impact of such internals on hydrodynamics and mass transfer for narrow columns, its role in pilot-scale columns is less clear. In this paper we report on a study of hydrodynamics and mass transfer in a BCR of 4.2 m height and 0.392 m diameter. We investigated different tube arrangements with triangular and square pitch and tube diameters of 32×10^{-3} m and 45×10^{-3} m at the same cross-sectional coverage (~25%). The column was operated at homogeneous and heterogeneous flow conditions. A customized three-layer wire-mesh sensor was utilized to visualize gas phase dynamics and liquid mixing characteristics in the column's cross-section. We found that sub-channel size is the most crucial geometric design parameter. Tracer mixing experiments reveal that internals enhance the liquid dispersion due to induction of large-scale liquid circulation. Mass transfer was studied with the oxygen stripping method. Here we found, that the effect of the internals on the gas-liquid mass transfer is almost negligible. Eventually, correlations for gas holdup, axial liquid dispersion and the volumetric gas-liquid mass transfer coefficient are given, which take the internals' geometry into account.

Keywords

Pilot-scale bubble column, Heat exchanger internals, Hydrodynamics, Liquid mixing, Mass transfer, Wire-mesh sensor

1 Introduction

Bubble column reactors (BCRs) are widely applied in the chemical process industry for a variety of processes, such as hydrogenation, nitrification or waste water treatment. They have a simple design and provide advantageous heat and mass transfer characteristics at comparably low energy input (Deckwer and Schumpe, 1993; Deckwer, 1992). To ensure high product selectivity, long catalyst lifetime as well as a safe and stable reactor operation, proper heat management is required for the mostly exothermic reactions (Rollbusch et al., 2015; Schlüter, 1992; Schlüter et al., 1995; Youssef et al., 2013). Different types of heat exchangers, such as jacket coolers (applicable for small reactors only), external heat exchangers and horizontal or vertical internal heat exchangers are typically used. The latter ones are the most common types as they provide a direct excess heat removal. As an example, in Fischer Tropsch reactors roughly 25% of the reactor's cross-sectional area (CSA) is covered by internal heat exchanger tubes. This has a considerable effect on gas-liquid dispersion and mixing characteristics (Hamed, 2012; Schlüter et al., 1995; Youssef et al., 2014). From previous studies (Berg, 1993; Bernemann, 1989; Bhusare et al., 2017; Forret et al., 2003; Guan and Yang, 2017; Guan et al., 2015, 2014; Guo and Chen, 2017; Kalaga et al., 2017; Laborde-Boutet et al., 2010; Larachi et al., 2006; Lau et al., 2018; Mesfer et al., 2017, 2016; Möller et al., 2018a, 2018b; Nedeltchev et al., 2018, 2017; Sultan et al., 2018a) the knowledge about the influence of internals can be summarized as follows.

- Internals promote bubble breakup and hence smaller bubbles with a narrow size distribution. This in turn increases gas holdup and interfacial area.
- Internals promote formation of large-scale liquid circulation cells with suppressed radial liquid dispersion due to the funneling effect caused by sub-channel bubble stabilization.
- Internals promote formation of wavy gas holdup profiles due to additional no-slip boundaries of the inserted tubes and occurrence of asymmetric flow patterns.
- Internals lead to lower gas-liquid mass transfer coefficients due to turbulence damping.

Most of the hydrodynamic properties in BCRs with internals have been studied in columns with inner diameters of 0.15 m and below (Hamed, 2012; Jasim, 2016; Kalaga et al., 2017; Mesfer et al., 2017, 2016; Sultan et al., 2018a, 2018b, 2018c; Youssef and Al-Dahhan, 2009; Youssef et al., 2013; Youssef, 2010). It is commonly agreed that main hydrodynamic characteristics of 0.15 m bubble columns resemble larger columns and, thus, are considered as the lower limit to derive reliable scale-up and design correlations (Wilkinson et al., 1992). This also coincides with the famous flow regime map of Shah et al. (1982), where the churn-turbulent flow regime does not evolve below this column diameter. However, recent experiments by Nedeltchev et al. (2018) in a narrow column with internals showed that the churn-turbulent flow regime is already reached in a column of only 0.1 m inner diameter, providing evidence that updated regime maps are needed for BCRs with internals. Furthermore, the formation of structures similar to Taylor flow at high superficial gas velocity instead of slug flow as in empty columns was observed within the sub-channels between internals of a narrow bubble column in our recent study

(Möller et al., 2018a). The tube coverage, which is typically 25 % of the CSA, obviously changes the scale-up conventions. However, it is not clear to which extent the main hydrodynamic characteristics as well as the flow regimes, and their boundaries, change with the column diameter.

Only a few studies explicitly addressed the effect of the diameter for columns larger than 0.15 m (Bernemann, 1989; Hamed, 2012; Yamashita, 1987; Youssef, 2010) and consistent conclusions can hardly be drawn. While Youssef (2010) and Hamed (2012) measured increasing gas holdup with increasing column diameter, Bernemann (1989) observed no effect and Yamashita (1987) even concluded that the gas holdup decreases with increasing column diameter. On the other hand, Youssef (2010) and Bernemann (1989) consistently observed enhanced large-scale liquid circulation with increasing column diameter.

Beyond these scale-up studies, the few available investigations on larger columns (Berg, 1993; Bernemann, 1989; Forret et al., 2003; Hamed, 2012; Westermeyer-Benz, 1992; Youssef, 2010) rely mostly on data from local probes placed at few positions only and flow asymmetries, known from narrow columns with internals (Jasim, 2016; Kalaga et al., 2018; Mesfer et al., 2017, 2016; Möller et al., 2018a, 2018b), were not detectable this way. Furthermore, to the best of the authors' knowledge, gas-liquid mass transfer in a pilot-scale BCR with internals has only been studied by Hamed (2012) using a column of 0.45 m diameter. However, the effects of internal size and tube pattern have not been addressed at all. Hitherto, design and scale-up correlations for columns with internals are hardly available, even less, taking the internals' geometry into account.

Thus, the objective of this work is to systematically quantify, for the first time, the effects of different internals patterns and tube sizes in a pilot-scale BCR on regime boundaries, gas holdup, bubble characteristics, liquid mixing patterns and gas-liquid mass transfer. Initially, main flow regime boundaries are identified based on the chaos theory to characterize the prevailing fluid dynamics and to compare with regime maps proposed for empty BCRs. The sub-channel gas phase dynamics and their contribution to the overall hydrodynamics will also be assessed. Eventually, correlations for gas holdup, gas-liquid volumetric mass transfer coefficient and axial liquid dispersion coefficient are proposed considering the most relevant geometrical parameters of the internals.

2 Experimental

2.1 Setup and internals design

In our study we used a segmented pilot-scale bubble column with an inner diameter of 0.392 m and a total height of 4.2 m. The sparger was designed to ensure bubble sizes and release frequencies comparable to our previous studies in a narrow bubble column of 0.10 m inner diameter (Lau et al., 2018; Möller et al., 2018a, 2018b; Nedeltchev et al., 2018, 2017). The number of holes in the sparger (860) was accordingly scaled, while hole size (0.5×10^{-3} m), triangular pitch (1×10^{-2} m) and total opening area ratio (0.14%) were kept the same. Figure 1 shows the experimental setup and CAD images of column and internals with details of internals' mounting (spacers) and wire-mesh sensor (WMS) installation.

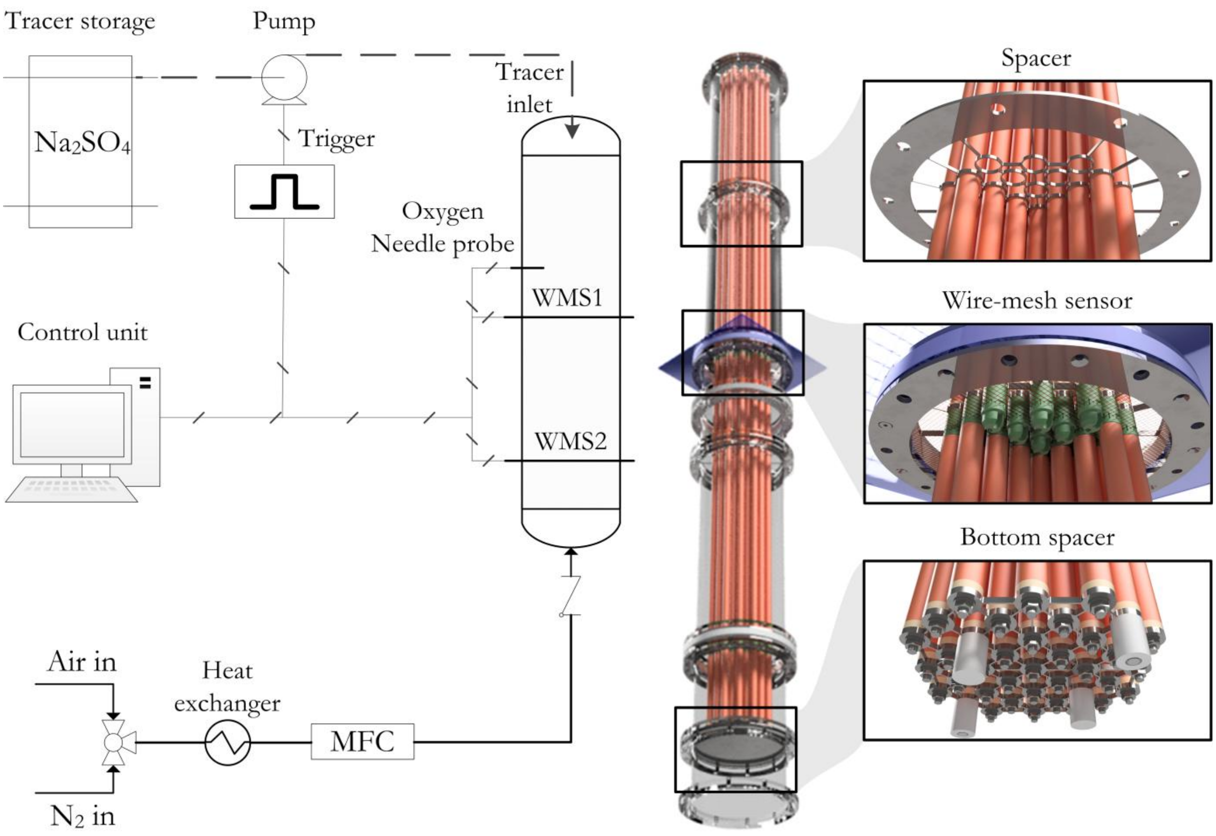
Tracer storage
Pump
Tracer inlet
Na_2SO_4
Trigger
Oxygen Needle probe
WMS1
Control unit
WMS2
Air in
Heat exchanger
MFC
N_2 in
Spacer
Wire-mesh sensor
Bottom spacer

Figure 1: Experimental setup and rendered CAD images of column and internals.

Four different configurations of the internals were applied for comparison with the empty column. The layout of the tubes and their specifications are summarized in Table 1.

Table 1: Summary of the internals' layout and design parameters.

Type	**Square 32 (s32)** 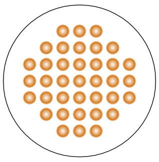	**Triangular 32 (t32)** 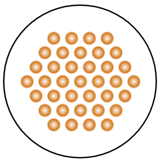	**Square 45 (s45)** 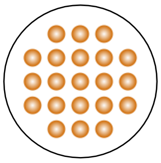	**Triangular 45 (t45)** 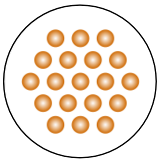
Tube outer diameter (d_o) in ×10^{-3}m	32	32	45	45
Pitch (P) in ×10^{-3}m	41.9.9	45.9	61.3	64.3
Hydraulic diameter (d_h) in ×10^{-3}m	28.7	22.2	41.9	31.0
Sub-channel area (A_s) in ×10^{-6}m^2	1034.3	511.7	2161.1	995.6

Coverage (A_c) in %	25	25	28	25
Number of tubes (N)	37	37	21	19

Two patterns (triangular and square pitches) were chosen, following the TEMA design for shell and tube heat exchangers (Shah and Sekulic, 2003; Thulukkanam, 2013). Furthermore, two tube sizes (32×10^{-3} and 45×10^{-3} m) were studied. The number of tubes was chosen to keep the coverage of the CSA approximately constant to ensure a heat removal capacity typical for Fischer-Tropsch reactors. The tubes were arranged sufficiently away from the column wall (r/R>0.75), which is standard in industry to ease the maintenance and to improve the heat transfer characteristics (Li and Prakash, 2001; Youssef, 2010). Five metal spacers (see images in Figure 1) were used to fix the tubes within the reactor.

Superficial gas velocities, u_g, (based on the free CSA) ranging from $0.01\,\mathrm{m\,s^{-1}}$ to $0.22\,\mathrm{m\,s^{-1}}$ were adjusted via mass flow controller (Omega, FMA 2613A). The range covers homogeneous and heterogeneous flow conditions. The gas temperature was adjusted to 20 °C via a heat exchanger to ensure a constant operating temperature. WMS working principle, data treatment and extraction of hydrodynamic parameters are explained below. The principles and data post-processing for liquid mixing and mass transfer measurements are described in detail elsewhere (Möller et al., (2018b).

2.2 Wire-mesh sensors for the study of hydrodynamics and liquid mixing

An in-house built conductivity WMS was used to measure gas phase dynamics (gas holdup, bubble characteristics, regime boundaries) and liquid mixing in the pilot-scale BCR. The WMS200 electronics with a capacity of 128 × 128 wires for operating the WMS was manufactured by Teletronic Rossendorf Ltd. A WMS typically consists of two planes with orthogonally arranged wires, where wires in one plane act as electrical transmitters and in the other one as receivers. The electrical resistance and, thus, the conductance in each virtual crossing point of the sensor are obtained at very high speed based on a multiplexing-excitation scheme. Liquid in the virtual crossing point returns high conductance (with a magnitude depending on the liquid conductivity), while gas returns zero conductance. This way, gas and liquid phases can be distinguished and conductivity tracer concentrations can be determined in the entire cross-section. The data can then be further post-processed to extract hydrodynamic and mixing parameters.

In this study, however, a three-layer sensor with an axial spacing of 4×10^{-3} m between each plane was built. The wires in the middle plane act as the transmitter and the two other wire-layers act as receivers (see Figure 2). This specific design enables simultaneous measurements in two nearby planes. Via cross-correlation of the phase signals from the two measurement planes, average phase velocities can be determined. Furthermore, by applying the bubble pairing algorithm proposed by Furuya et al. (2017), the velocity information of rising and descending gas bubbles is evaluated.

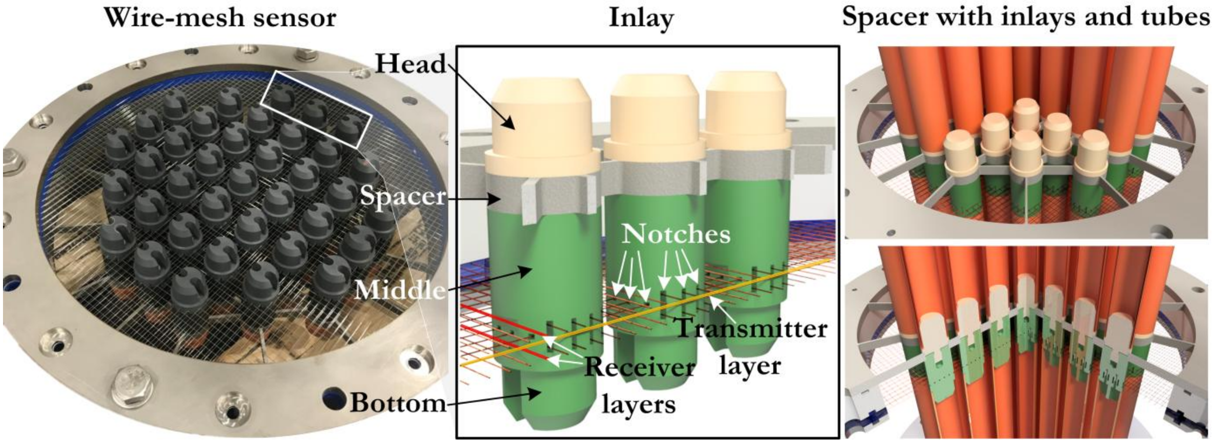

Figure 2: Photograph of the WMS with rendered CAD images of inlays, spacers and tubes.

To mount the WMS within the tube bundle, special inlays were designed, which have the spacing of the wires milled into them. A CAD image of such inlay is shown in Figure 2. To avoid any mechanical stress on the wires, a streamlined spacer is flange-mounted 5×10^{-2} m above the WMS and takes up the forces resulting from the weight of tubes and inlays. Similar WMS studies in a small rod bundle mock-up were conducted by Ylönen (2013).

The three planes of the WMS consist of 64 wires each, installed with a lateral spacing of 6.125×10^{-3} m, which defines the lower size limit of gas structures that can be properly measured. Gas structures smaller than the wire-spacing are characterized by their chord length (Beyer et al., 2018).

The WMS was installed at a height of L_s/D = 5.1, which is well above the entrance length to ensure representative results (Wilkinson et al., 1992). The WMS measurements for liquid mixing were conducted at a height of $L_s/L_d \approx$ 0.8 as proposed by Deckwer (1992). The total measurement times for gas phase dynamics/regime transition and liquid mixing experiments were 24 s and 180 s, respectively, at an imaging frequency of 2500 frames s^{-1}.

For the liquid mixing measurements, 5×10^{-3} L Na_2SO_4 (sodium sulfate) solution (0.4 mol L^{-1}) was injected for a pulse duration of 1.0 s on top of the gas-liquid dispersion in the center of the column via dosing pump (ISMATEC ISM446, controlled by an Agilent 33250A signal generator). Tracer injection and WMS measurement were simultaneously triggered via in-house developed trigger device (clock box (HZDR Innovation, 2013)). All tracer measurements were repeated three times. Results for the two adjacent planes were simultaneously obtained from the three layered WMS.

2.3 Oxygen probe and gas-liquid mass transfer measurement procedure

For mass transfer analysis we used an oxygen needle probe (Unisense Ox100) at r/R = 0.9 (the wall region outside of the tube bundle) at a height of L_c/D = 6.2 above the gas sparger. At first, the column was flushed with nitrogen to fully strip the oxygen from the deionized water. Subsequently, a three way valve was switched from nitrogen to pressurized air and the oxygen uptake was recorded. Depending on the superficial gas velocity, the measurement time varied between 60 s and 240 s until oxygen saturation was reached. Each measurement was repeated three times with the identical procedure.

3 Data post-processing and parameter extraction

3.1 Gas holdup

The WMS receiver measures a current driven by the activated transmitter wire, which is subsequently converted into a voltage signal, amplified and converted to a digital value (ADC). Hence, local instantaneous gas holdup, $\varepsilon_{i,j,k}$, is calculated using the WMS two-phase flow ADC-values, $U_{\mathrm{m,i,j,k}}$, and the bulk phase (water) reference, $U_{w,i,j}$, without imposed gas flow according to

$$\varepsilon_{i,j,k} = \frac{U_{w,i,j} - U_{m,i,j,k}}{U_{w,i,j}} = 1 - \frac{U_{m,i,j,k}}{U_{w,i,j}}, \tag{1}$$

where i and j indicate the respective virtual wire crossing point and k represents the measurement frame. The resulting gas holdup data are filtered to eliminate signal noise (Beyer et al., 2018). The time-averaged local gas holdup is calculated as

$$\varepsilon_{\mathrm{g},i,j} = \frac{1}{k_{\max}} \sum_{k=1}^{k_{\max}} \varepsilon_{i,j,k}, \tag{2}$$

where $k_{\max} = 60{,}000$ is the maximum number of frames. The total gas holdup, ε_{g}, is calculated averaging the local data according to

$$\varepsilon_{\mathrm{g}} = \sum_{i=1}^{n_{\mathrm{w},i}} \sum_{j=1}^{n_{\mathrm{w},j}} \varepsilon_{\mathrm{g},i,j}\, a_{i,j}, \tag{3}$$

where $n_{\mathrm{w},i}$ or $\mathrm{n}_{\mathrm{w},j}$ are the respective wires in i and j direction. The weighting factor for each crossing point, $a_{i,j}$, is calculated as

$$a_{i,j} = \frac{A_{\mathrm{p}}}{A_{\mathrm{t,f}}}, \tag{4}$$

where A_{p} is the area of one pixel usually by the lateral wire-spacing and $A_{\mathrm{t,f}}$ is the total free pixel area, e.g. the area not covered by the inlays. Obviously, the weighting factor for pixels, which are in the vicinity of the tube inlays, have smaller values compared to weighting factors for pixels, which are in the free area. All weighting factors sum up to a total value of 1. The weighting factor is determined with the help of the geometry post processing tool for WMSs, which is described in more detail elsewhere (Beyer et al., 2018).

3.2 Bubble size distribution

Individual bubbles are detected from the 3D data matrix, where each bubble comprises a cluster of n_b voxels. The dimension of a voxel is $l_V^2 \cdot v_{\mathrm{b}} \cdot \Delta t$, with the voxel edge length $l_V = 6.125\times10^{-3}\,\mathrm{m}$, the time between two subsequent images $\Delta t = 5\times10^{-3}\,\mathrm{s}$ and the bubble velocity, v_{b}. Accordingly, the bubble volume is

$$V_{\mathrm{b}} = n_{\mathrm{b}} \cdot l_V^2 \cdot v_{\mathrm{b}} \cdot \Delta t \quad . \tag{5}$$

Assuming a spherical bubble shape, the equivalent diameter can be calculated as

$$d_{\mathrm{e}} = \left(\frac{6\,V_{\mathrm{b}}}{\pi}\right)^{\frac{1}{3}}. \tag{6}$$

It should be mentioned that the determined bubble diameter is a rather rough estimation considering arbitrary bubble shapes. However, the resulting bubble size distributions yet reveal the effect of the internals on the predominance of bubble breakup or coalescence.

More information about the post-processing of WMS data can be found elsewhere (Furuya et al., 2017; Kipping et al., 2017, 2016; Prasser et al., 1998).

3.3 Gas phase velocity

The velocity of the gas phase, i.e. bubble velocity, v_{b}, can be determined individually for every bubble via bubble pairing or in a time-averaged manner via cross-correlation. The latter is used to scale the z-axis of the pseudo-3D data for a proper bubble size determination (see Section 3.2).

The average bubble velocity is determined for every virtual crossing point by cross-correlating the signals of the two planes to obtain their time offset. The cross-correlation procedure for the determination of the axial gas velocity in the column cross-section is schematically shown in Figure 3.

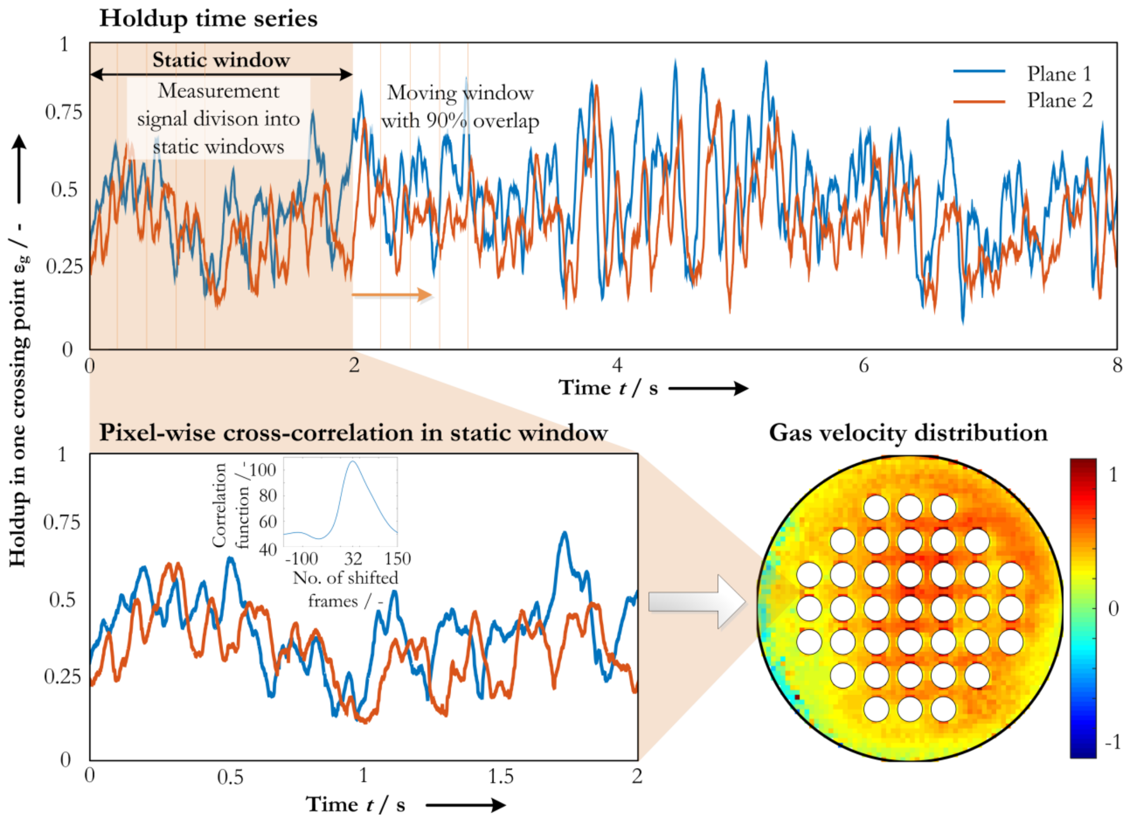

Figure 3: Illustration of the pixel-wise cross-correlation procedure for the gas holdup time series of the two measurement planes.

To capture the characteristic flow structures of the stochastic bubbly flow (e.g. small bubbles move within a liquid circulation cell and have various turbulence spectra at different scales) with dynamically changing asymmetric flow patterns, the 24 s measurement signals of both planes were divided into segments (windows) of different lengths between 0.25 s and 12 s (i.e. 625 to 30,000 frames), depending on prevailing time-scale and superficial gas velocity, and cross-correlated in a pixel-wise manner. The window size was chosen to minimize the gas phase mass balance error according to

$$u_g = \frac{1}{N_\mathrm{v}} \cdot \sum_{i=1}^{i=n_{\mathrm{w},i}} \sum_{j=1}^{j=n_{\mathrm{w},j}} u_{\mathrm{g}_{i,j}} \cdot \varepsilon_{\mathrm{g}_{i,j}}\,, \tag{7}$$

where N_v is the number of valid (i.e. not embedded within the inlays) virtual wire crossing points. It should be mentioned that the window was always shifted with an overlap of 90%.

The bubble pairing algorithm was, in turn, used for the determination of individual bubble velocities within the sub-channels of the internals. Here, bubbles moving from plane to plane are tracked using the pairing algorithm of Furuya et al. (2017) based on the following pairing criteria:

- time lag between detection at both planes $|\Delta t| \leq 0.04$ s, which equals 100 frames,

- lateral shift of the tracked bubble $\Delta d \leq 8\times10^{-3}$ m, which is chosen according to the lateral wire-spacing, and
- volume change of the tracked bubble $\Delta r_\mathrm{V} \leq 0.2$, which is the ratio of the bubble volume in the respective planes.

From the bubble pairs, the axial velocity component is eventually derived.

3.4 Liquid mixing and mass transfer coefficient

Gas-liquid mass transfer coefficients as well as radial and axial liquid dispersion coefficients from oxygen probe and WMS data, respectively, are derived according to the procedure explained in our recent article (Möller et al., 2018b).

The WMS data from tracer pulse injections were cropped (envelope filtering to cut off signal bumps caused by passing bubbles) and normalized (scaling between 0 and 1). Subsequently, the axial and radial dispersion coefficients were determined by fitting the experimental data in a radially symmetric manner to the 2D dispersion model according to

$$\frac{\partial c_\mathrm{l}}{\partial t} = D_{\mathrm{z,l}}\frac{\partial^2 c_\mathrm{l}}{\partial z^2} - u_\mathrm{l}\frac{\partial c_\mathrm{l}}{\partial z} + \frac{D_{\mathrm{r,l}}}{r}\frac{\partial c_\mathrm{l}}{\partial r} + D_{\mathrm{r,l}}\frac{\partial^2 c_\mathrm{l}}{\partial r^2}. \tag{8}$$

$D_{\mathrm{z,l}}$ and $D_{\mathrm{r,l}}$ denote the axial and radial liquid dispersion coefficients, r is the radial position in the reactor's cross-section and u_l is the superficial liquid velocity (zero for batch operation). An analytical solution was derived by Rubio et al. (2004) using the Danckwert's boundary conditions (zero gradient boundary) according to

$$c_\mathrm{T}(x,y) = \left(\sum_{m=1}^{\infty}\frac{J_0(\nu_\mathrm{m} r^*)}{J_0(\nu_\mathrm{m} R^*)}\cdot\exp(-\nu_\mathrm{m}^2 t^*)\right)\left(1 + 2\sum_{n=1}^{\infty}[(\cos n\pi z^*)\cdot\exp(-n^2\pi^2 t^*)]\right) \tag{9}$$

with

$$t^* = \frac{D_{\mathrm{z,l}} t}{{L_\mathrm{d}}^2}, z^* = \frac{z}{L_\mathrm{d}}, r^* = \frac{r}{L_\mathrm{d}}\sqrt{\frac{D_{\mathrm{z,l}}}{D_{\mathrm{r,l}}}}, R^* = \frac{R}{L_\mathrm{d}}\sqrt{\frac{D_{\mathrm{z,l}}}{D_{\mathrm{r,l}}}}. \tag{10}$$

The dimensionless tracer concentration, c_T, (also called mixing scalar) depends on dimensionless time, t^*, dimensionless axial position, z^*, and dimensionless radial position, r^*, as well as the dimensionless radius, R^*. J_0 is the zero-order Bessel function and ν_m is the m^th root of the first-order Bessel function. If

$D_{\mathrm{r,l}} \gg D_{\mathrm{z,l}}$, only axial dispersion determines mixing and Equation 9 approaches the analytical solution for the 1D axial dispersion model (Ohki and Inoue, 1970).

To determine the gas-liquid mass transfer characteristics, the oxygen concentration data were first deconvolved using the response time constant to obtain instantaneous $k_{\mathrm{l}}a$ values as described by Han and Al-Dahhan (2007) according to

$$\frac{dc_{\mathrm{s}}}{dt} = K_{\mathrm{s}}(c_{\mathrm{l}} - c_{\mathrm{s}}), \tag{11}$$

where c_{l} is the bulk concentration, c_{s} is the concentration measured at the sensor tip and K_{s} is the probe constant. This constant is determined experimentally from the first order response delay rapidly switching the sensor from oxygen-saturated to nitrogen-saturated water. A value of 1.5 s^{-1} was determined for the probe time constant.

According to Deckwer et al. (1983), Han and Al-Dahhan (2007) and Hamed (2012), the volumetric gas-liquid mass transfer coefficient in bubble columns depends on the degree of liquid backmixing superimposed to plug flow as determined via liquid mixing experiments explained above. Thus, the volumetric gas-liquid mass transfer coefficient can be calculated using the axial dispersion model according to

$$\begin{aligned} \frac{dc_{\mathrm{g}}}{dt} &= D_{\mathrm{z,g}}\frac{d^2c_{\mathrm{g}}}{dz^2} - \frac{u_{\mathrm{g}}}{\varepsilon_{\mathrm{g}}}\frac{dc_{\mathrm{g}}}{dz} - \frac{k_{\mathrm{l}}a}{\varepsilon_{\mathrm{g}}}\left(Hc_{\mathrm{g}} - c_{\mathrm{l}}\right), \\ \frac{dc_{\mathrm{l}}}{dt} &= D_{\mathrm{z,l}}\frac{d^2c_{\mathrm{l}}}{dz^2} + \frac{k_{\mathrm{l}}a}{\varepsilon_{\mathrm{l}}}\left(Hc_{\mathrm{g}} - c_{\mathrm{l}}\right). \end{aligned} \tag{12}$$

H is the Henry constant and c_{g} and c_{l} are the gas and liquid oxygen concentrations. While the liquid dispersion coefficient, $D_{\mathrm{z,l}}$, was extracted from the WMS data (see Equation 9), the axial gas dispersion coefficient, $D_{\mathrm{z,g}}$, was correlated according to Wachi and Nojima (1990) as

$$D_{\mathrm{z,g}} = 20u_{\mathrm{g}}D^{1.5}. \tag{13}$$

It should be noted that gas phase dispersion data for bubble columns are rarely available. The gas dispersion coefficient is crucial for a correct determination of the mass transfer coefficient, however, it can vary over several orders of magnitude depending on the selected correlation as highlighted by Döß et al. (2017). Thus, the correlation of Wachi and Nojima (1990), which was developed based on experiments performed at comparable dimensions and throughputs, was considered.

4 Results

4.1 Gas phase dynamics

4.1.1 Flow regime transition

To assess the impact of internals on the flow regimes, in particular on the transition between homogeneous and heterogeneous flow, e.g. slug flow or churn-turbulent flow, the Kolmogorov entropy (KE) method was used, which is considered the most reliable and well-reported regime-identifier approach (Nedeltchev and Shaikh, 2013; Nedeltchev, 2009; Nedeltchev et al., 2017, 2014; Schouten et al., 1994). To calculate the KE, the time series of the cross-sectional averaged gas holdup is split into numerous state vectors each with 50 elements, which is also called the embedding dimension. The cut-off length, which is a key parameter of the KE algorithm, was set as the average absolute deviation from the time series (Schouten et al., 1994). In Figure 4 the KE is exemplary shown as a function of the superficial gas velocity for the empty BCR and the Triangular 45 (*t45*) configuration.

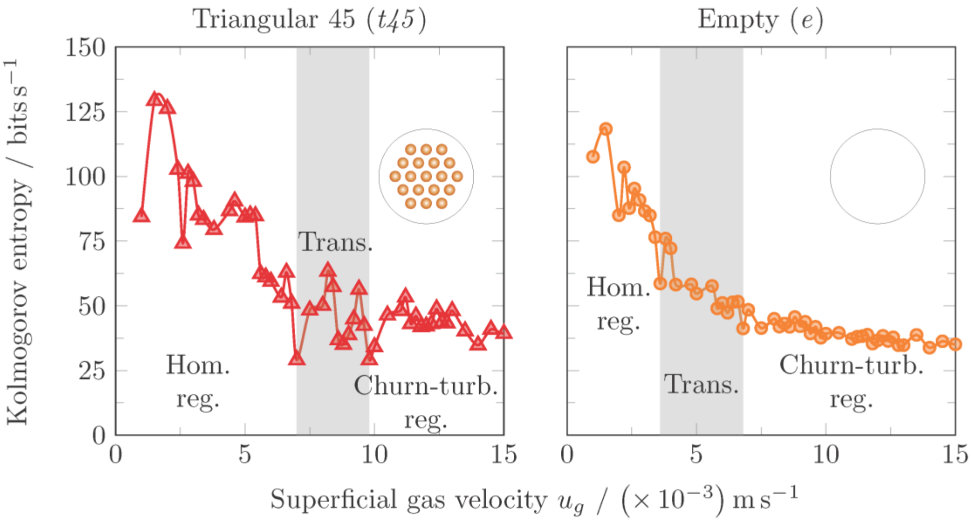

Figure 4: Examples for the regime transition derived from Kolmogorov entropy for Triangular 45 (*t45*) configuration and empty bubble column.

The KE analysis returns global minima as identifiers for regime boundaries and local minima as identifiers for sub-regime boundaries (not specified in Figure 4) (Nedeltchev et al., 2014). The transition, separating homogeneous and heterogeneous flow regimes, can be clearly identified. From Figure 4 it is evident that internals alter the onset of the particular regimes. The Triangular 45 (*t45*) internals extend the homogeneous flow regime and shift the transition to heterogeneous flow regime towards higher superficial gas velocities due to the bubble caging within the sub-channels suppressing and delaying the formation of large bubbles.

Figure 5 summarizes the identified transition velocities for the columns with and without internals studied at pilot-scale (0.392 m) as well as for the narrow column (0.1 m) from previous measurements (Lau et al., 2018; Möller et al., 2018a, 2018b; Nedeltchev et al., 2018, 2017) in a modified map derived from the renowned flow regime map of Shah et al. (1982).

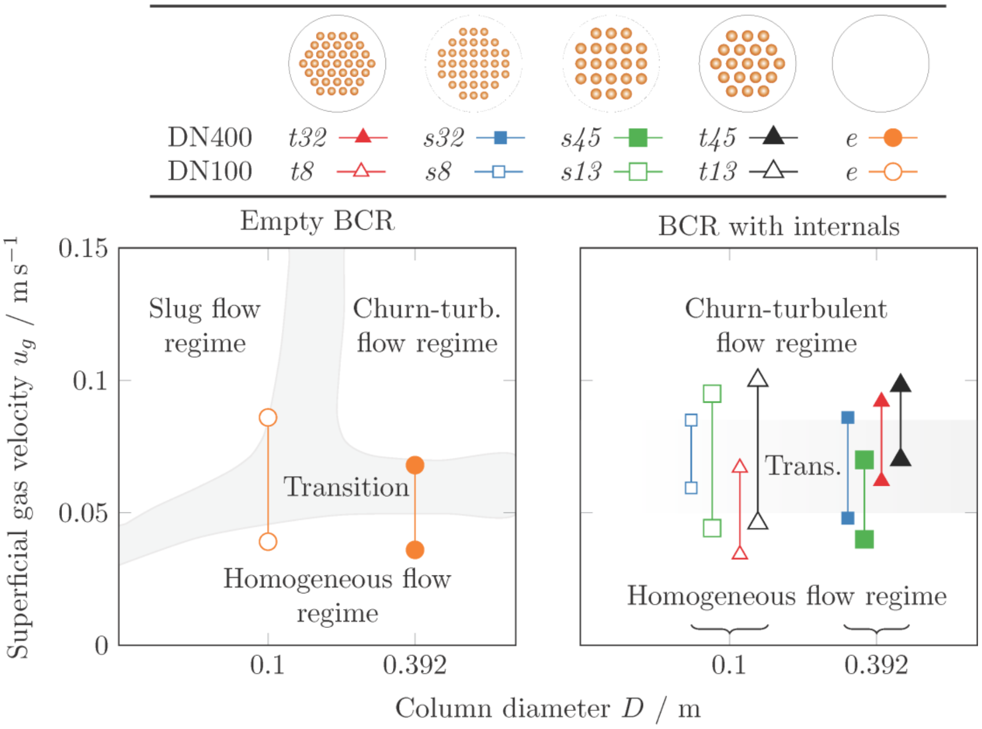

Figure 5: Regime transitions for left) the empty BCR inserted in the map of Shah et al. (1982) and right) BCRs with internals inserted in a modified flow regime map.

The regime transitions for the empty columns agree fairly well with the transitions proposed by Shah et al. (1982). Except for the Triangular 8 (*t8*) and Square 45 (*s45*) configurations, the internals stabilize the homogeneous flow regime and shift the end of the homogeneous flow regime and the onset of the churn-turbulent flow regime towards higher superficial gas velocities. The earlier transition for the Triangular 8 (*t8*) configuration in the narrow column results from the very small hydraulic sub-channel (d_h = 5.6×10^{-3} m), forcing the bubbles to accumulate and preferably rise in the wall region accompanied by forced bubble coalescence and, thereby, the formation of large bubbles. The Square 45 (*s45*) configuration, on the other hand, has a large hydraulic sub-channel diameter (d_h = 41.9×10^{-3} m), which stabilizes the formation of large Taylor-bubbles within the bundle which, in turn, shift the regime transition towards lower superficial gas velocities.

The effect of column diameter on the regime transition for columns with internals is significant, however, the differences between narrow and pilot-scale column depend on the configuration. Whereas the regime transition onset shifts towards higher superficial gas velocities with increasing column diameter for the triangular configurations (*t8, t13, t32, t45*), the opposite trend is obtained for the square configurations (*s8,* *s13, s32, s45*). As mentioned above, the triangular sub-channels in the narrow column are very small, resulting in bubble movement towards the wall immediately after their release from the sparger. This leads to the formation of bubble agglomerates and an early regime transition onset. With increasing column and tube diameter, the sub-channel size increases, too, which forces the bubbles to move within the bundle and, hence, the regime transition onset is delayed. For the square configurations, on the other hand, the sub-channel diameters for the pilot-scale column stabilize large Taylor-bubbles, which, in turn, results in an early regime transition onset.

Based on the identified regime boundaries, evolving gas holdup profiles and BSDs in the column as well in individual sub-channels are discussed mainly at superficial gas velocities particularly assigned to homogeneous, transition and heterogeneous flow regime at superficial gas velocities of 0.02 m s^{-1}, 0.06 m s^{-1} and 0.15 m s^{-1}, respectively.

4.1.2 Gas holdup

Figure 6 summarizes the gas holdup for all internals configurations in the pilot-scale column compared to the column without internals. Bubble breakup for BCRs with internals is the prevailing mechanism, returning smaller bubbles and, hence, higher gas holdups. The decisive geometrical parameters for the gas holdup are hydraulic sub-channel diameter and area. The Triangular 45 (*t45*) and the Square 32 (*s32*) configurations have approximately the same hydraulic sub-channel diameter and area (*t45*: d_h = 31.0×10^{-3} m, A_s = 995.6×10^{-6} m^2; *s32*: d_h = 28.7×10^{-3} m, A_s = 1034.3×10^{-6} m^2), which promote bubble breakup and decrease the flow friction. Thus, bubbles preferably rise within the tube bundle. While for small hydraulic sub-channels, e.g. Triangular 32 (*t32)*, the flow friction increases and bubbles are pushed towards the column's wall forming bubble clusters, large sub-channels, e.g. Square 45 (*s45*), stabilize large Taylor-bubbles. Both effects result in a gas holdup decrease.

Gas holdup peaks appear between superficial gas velocities of 0.05 and 0.07 m s^{-1}. Such behavior is very common for spargers with holes below 1×10^{-3} m in diameter (Sharaf et al., 2016) with mono-dispersed initial bubble size, which causes the hindrance effect. Here, bubbles in the homogeneous flow regime mutually affect their rise velocity, which leads to a convex holdup slope as a function of the superficial gas velocity as also discussed by Besagni et al. (2017) and Sharaf et al. (2016). However, for the Square 45 (*s45*) configuration, the large hydraulic diameter, which features wide BSDs, suppresses the hindrance effect counteracting the formation of such peak.

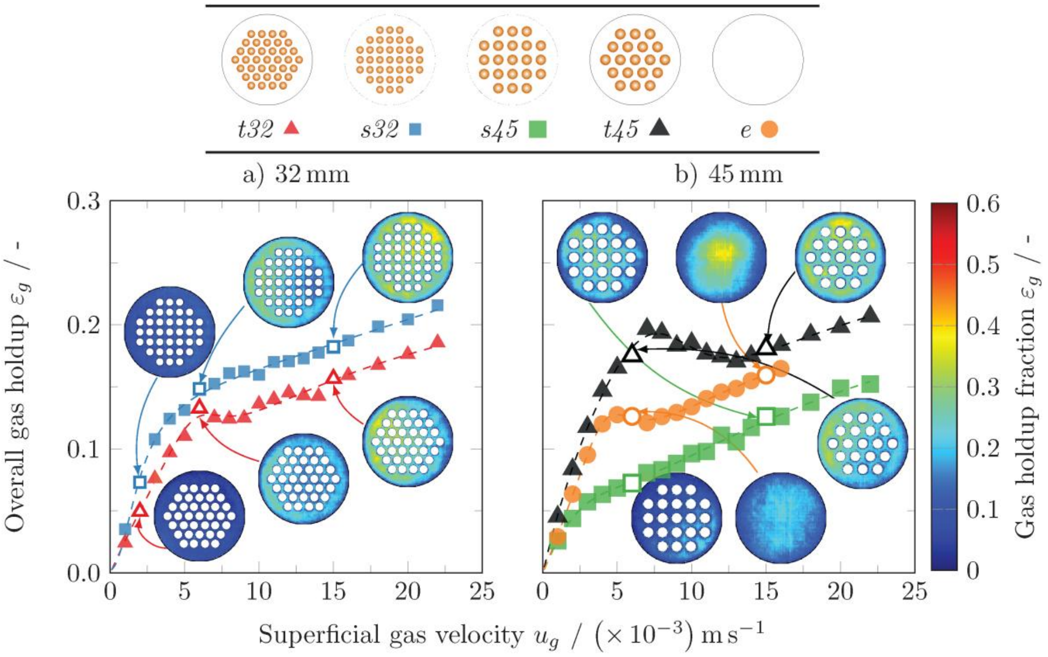

Figure 6: Total gas holdup depending on of the superficial gas velocity for aquare and triangular patterns for a) 32 mm b) 45 mm tubes with characteristic gas holdup patterns covering homogeneous (0.02 m s^{-1}), transition (0.06 m s^{-1}) and heterogeneous flow regime (0.15 m s^{-1}).

Comparing the data with our previous studies in the narrow column (0.1 m I.D.) (Lau et al., 2018; Möller et al., 2018a), lower gas holdups are obtained in the churn-turbulent regime, which is clearly attributed to the larger sub-channel area. The same results for the effect of the column diameter were found by Yamashita (1987).

The embedded gas holdup plots in Figure 6 confirm the typical parabolic distribution for the empty BCR, while internals promote flow asymmetries also known from narrow columns (Jasim, 2016; Kalaga et al., 2018; Mesfer et al., 2017, 2016; Möller et al., 2018a, 2018b). Such asymmetries may provoke concentration gradients and hotspots with the risk of rapid catalyst deactivation or product selectivity losses. Exemplary, evolving holdup profiles and accompanied asymmetries are also shown along a central line through the CSA for Square 32 (*s32*) configuration and empty column at superficial gas velocities of 0.02, 0.06 and 0.15 m s^{-1} covering homogeneous, transition and heterogeneous flow regimes, respectively (Figure 7).

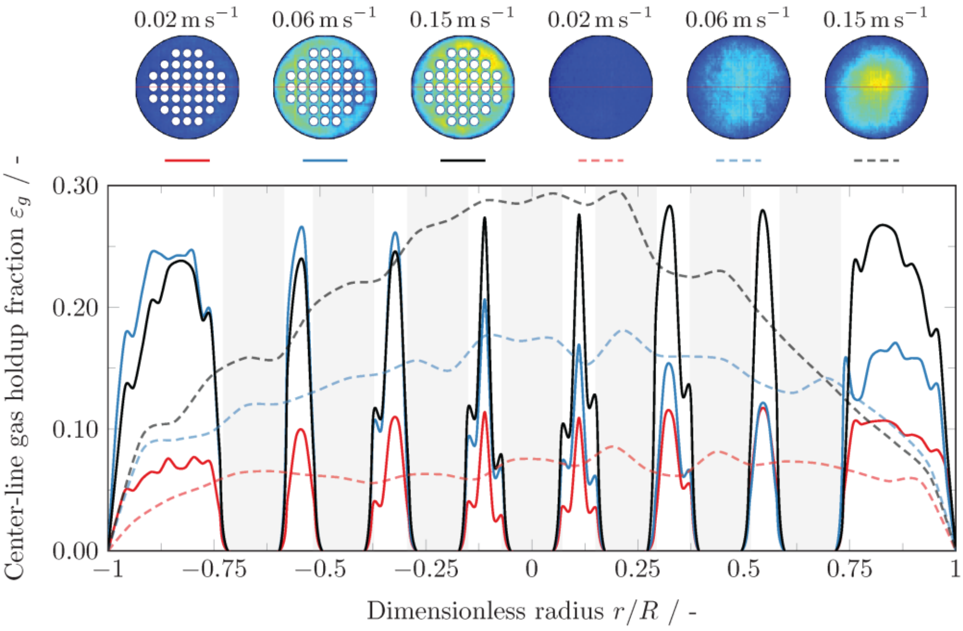

Figure 7: Center-line gas holdup for Square 32 (*s32*) configuration and empty column for gas velocities covering homogeneous, transition and heterogeneous flow regime.

For the empty BCR, the well-known parabolic holdup shape evolves, where large bubbles rise in the center of the column and small bubbles recirculate in the wall region due to pressure and velocity gradients. The internals moderately homogenize the gas holdup (considering the maxima within the sub-channels). In the sub-channels between the internals, however, parabolic holdup profiles shape as a result of the no-slip boundary conditions at the tube walls. Furthermore, the center-line profiles reveal that flow asymmetries mainly occur at conditions assigned to the regime transition ($0.06\,\mathrm{m\,s^{-1}}$), while churn-turbulent flow conditions ($0.15\,\mathrm{m\,s^{-1}}$) stabilize the flow and minimize the risk for hotspot formation.

4.2 Bubble characteristics

4.2.1 Bubble size distribution, Sauter mean diameter and interfacial area

In Figure 8, the cross-sectional, time-averaged volumetric BSD is shown for homogeneous, transition and heterogeneous flow regimes. The narrow BSD at homogeneous bubbly flow widens towards the heterogeneous regime caused by breakup and coalescence events. While internals with small tubes do not significantly alter the BSD, the bundle layout with 45 mm tubes widens the size spectra. This is particularly the case for the Square 45 (*s45*) configuration due to the formation of large bubbles and their stabilization within the sub-channels as a result of the larger sub-channel size ($d_\mathrm{h} = 42\times10^{-3}\,\mathrm{m}$). For all other configurations, bubble breakup is the main bubble formation mechanism with slightly narrower BSD compared to the empty BCR.

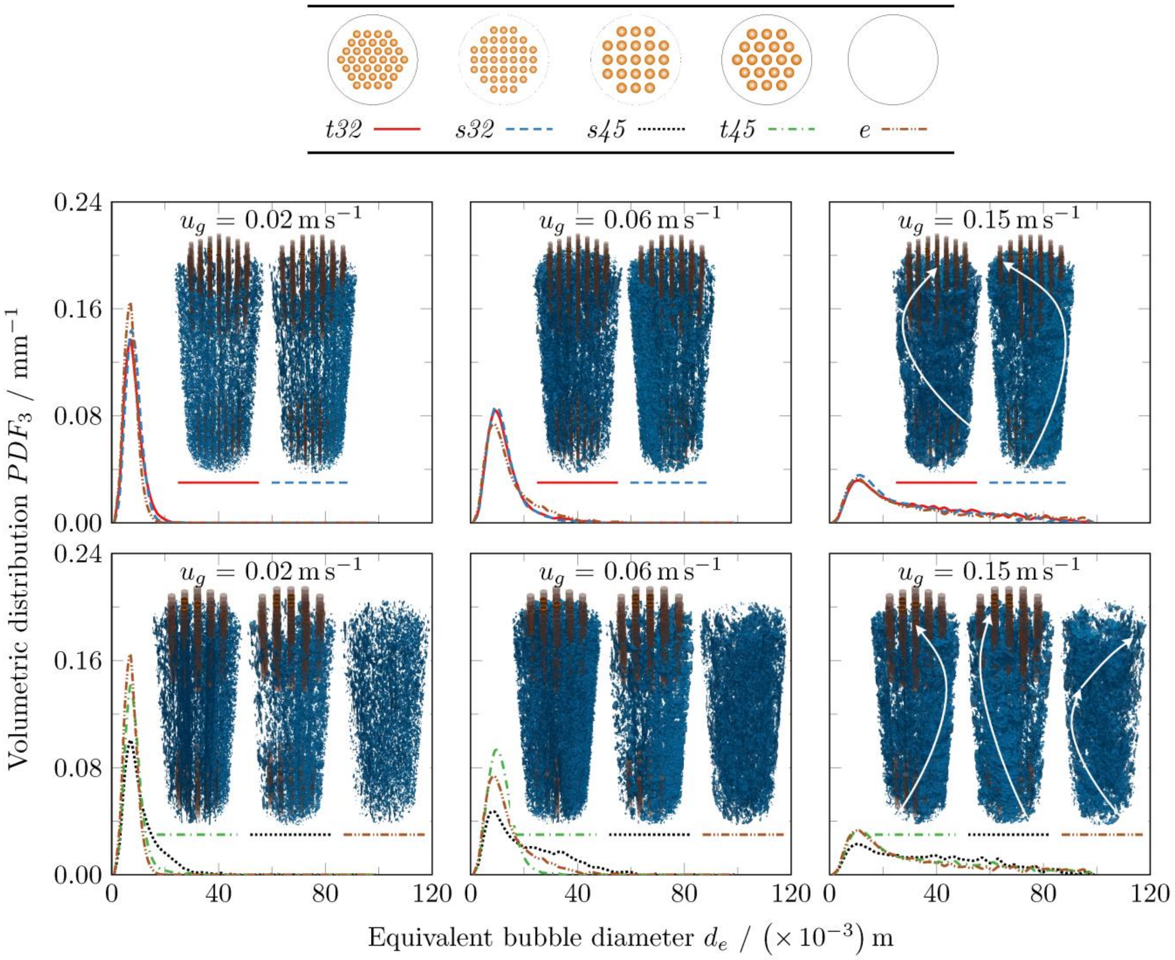

Figure 8: Bubble size distribution at homogeneous, transition and heterogeneous flow regime for 32 mm (upper row) and 45 mm (lower row) tubes (larger images of the pseudo 3D structures are provided as Supplementary Material).

For low superficial gas velocities, the flow structure is regular and the gas phase is uniformly distributed within the cross-section (see embedded pseudo 3D structures shown for 1 s), which is known for the homogeneous flow regime. With increasing superficial gas velocity, larger bubbles form and rise in a helical manner (white arrows in Figure 8). Compared to the empty column, the flow structure for BCRs with internals is more ordered due to the funneling effect (suppression of radial bubble exchange) of the sub-channels.

The bubble size distribution can be further characterized by means of the Sauter mean diameter (Figure 9, upper row) and interfacial area (Figure 9, lower row). Here, the Sauter mean diameter was calculated according to Lau et al. (2018) based on the bubble perimeter detection from every image without considering the individual bubbles speed. Subsequently, the interfacial area was determined according to $a = 6\varepsilon_\mathrm{g}/d_{32}$.

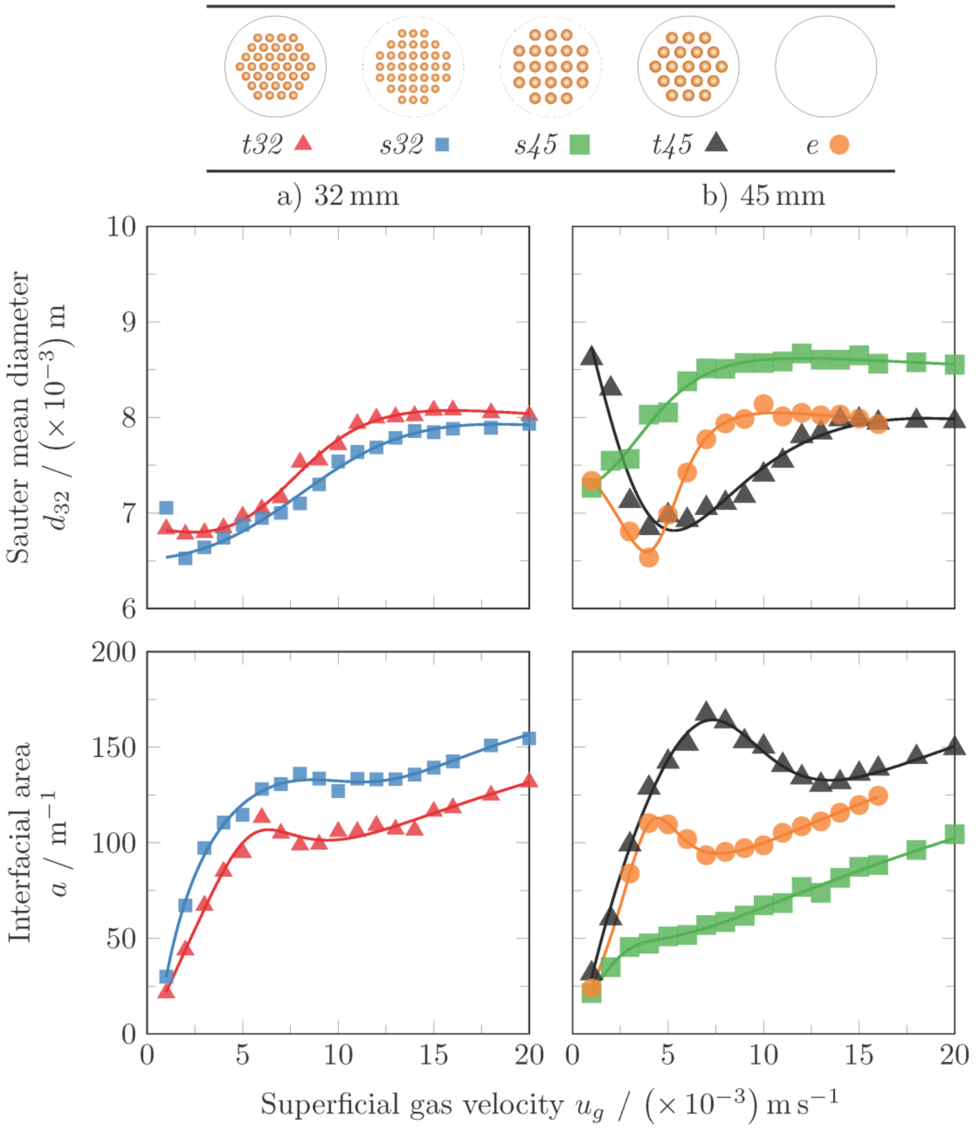

Figure 9: Sauter mean diameter and interfacial area as a function of the superficial gas velocity for a) 32 mm tubes and b) 45 mm tubes.

As mentioned above, bubbles smaller than ~ 6×10^{-3} m are not properly captured by the WMS and, thus, approximated by their chord lengths. Accordingly, the Sauter mean diameter and the interfacial area might be slightly over- and underestimated, respectively.

Generally, the Sauter mean diameter is smaller and the interfacial area is higher for BCRs with internals, which is in line with the literature (Berg, 1993; Youssef, 2010). For the empty and the Triangular 45 (*t45*) configuration, the Sauter mean diameter firstly decreases with increasing superficial gas velocity, which can be attributed to stronger liquid turbulent fluctuations (Deckwer et al., 1978). This, in turn, results in a large interfacial area. As of a superficial gas velocity of 0.04 m s^{-1}, the Sauter mean diameter increases up to $u_g = 0.10$ m s^{-1} and remains rather constant beyond, which is due to a stabilization effect of the sub-channels on the bubble formation and breakup and coalescence being in equilibrium.

The Triangular 45 (*t45*) configuration causes the highest interfacial area, which can be attributed to the highest breakup frequency resulting in the smallest Sauter mean diameter as well as the highest total gas holdup (see Figure 6). However, the large sub-channels of the Square 45 (*s45*) configuration stabilize large bubbles, resulting in increasing Sauter mean diameters, decreasing holdups and, hence, decreasing interfacial areas.

In our previous study (Lau et al., 2018; Möller et al., 2018a), a decreasing Sauter mean diameter was observed for increasing superficial gas velocity as a result of the sub-channel wall stabilization effect of small bubbles in narrow columns. At the pilot-scale, this effect is less effective due to the larger sub-channel areas.

4.2.2 Bubble size distribution within the sub-channels

Figure 10 summarizes the BSDs exemplary in center and wall sub-channels within the Square 32 and 45 (*s32*, *s45*) internals at homogeneous, transition and heterogeneous flow regimes. The sub-channel position was found to have no particular effect; thus, data from one channel properly characterizes the flow within the tube bundle.

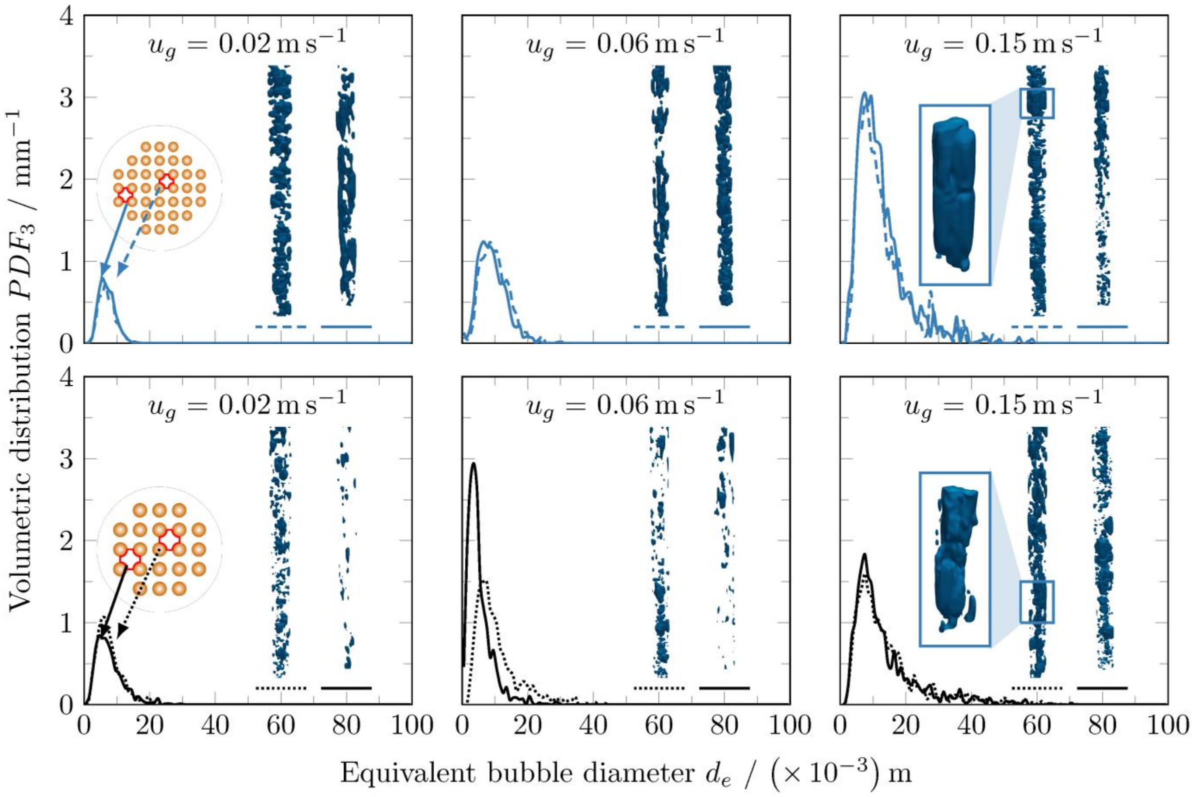

Figure 10: Bubble size distribution within the center and wall sub-channels for the Square 32 (top row) and 45 (bottom row) configurations as a function of the flow regime.

The BSDs from the different patterns reveal that the size of the sub-channel governs the size of the bubbles. Gas structures similar to Taylor-bubbles evolve at high superficial gas velocities in all internals (the structure of the sub-channel shapes the bubbles). This phenomenon was also reported in a recent study for a narrow column (Möller et al., 2018a, 2018b). The formation of such structures leads to the development of local liquid recirculation zones within the sub-channel and the neighboring tubes, hence an inhibition of radial bubble exchange. In addition, bubble velocity information (not shown here) reveal ascending and descending bubbles within the sub-channels, which follow local recirculation zones enforced by the complex flow pattern for BCRs with internals.

4.3 Liquid mixing and gas-liquid mass transfer

4.3.1 Liquid mixing

The liquid mixing efficiency is characterized via axial and radial dispersion coefficients, D_{z} and D_{r}, as well as mixing time. Figure 11 summarizes the determined dispersion coefficients for all internals' configurations as well as for the empty column. It should be mentioned that the obtained radial dispersion coefficient for the empty column is not shown here as the flow is mainly controlled by axial dispersion $(D_{\mathrm{r}} \gg D_{z})$.

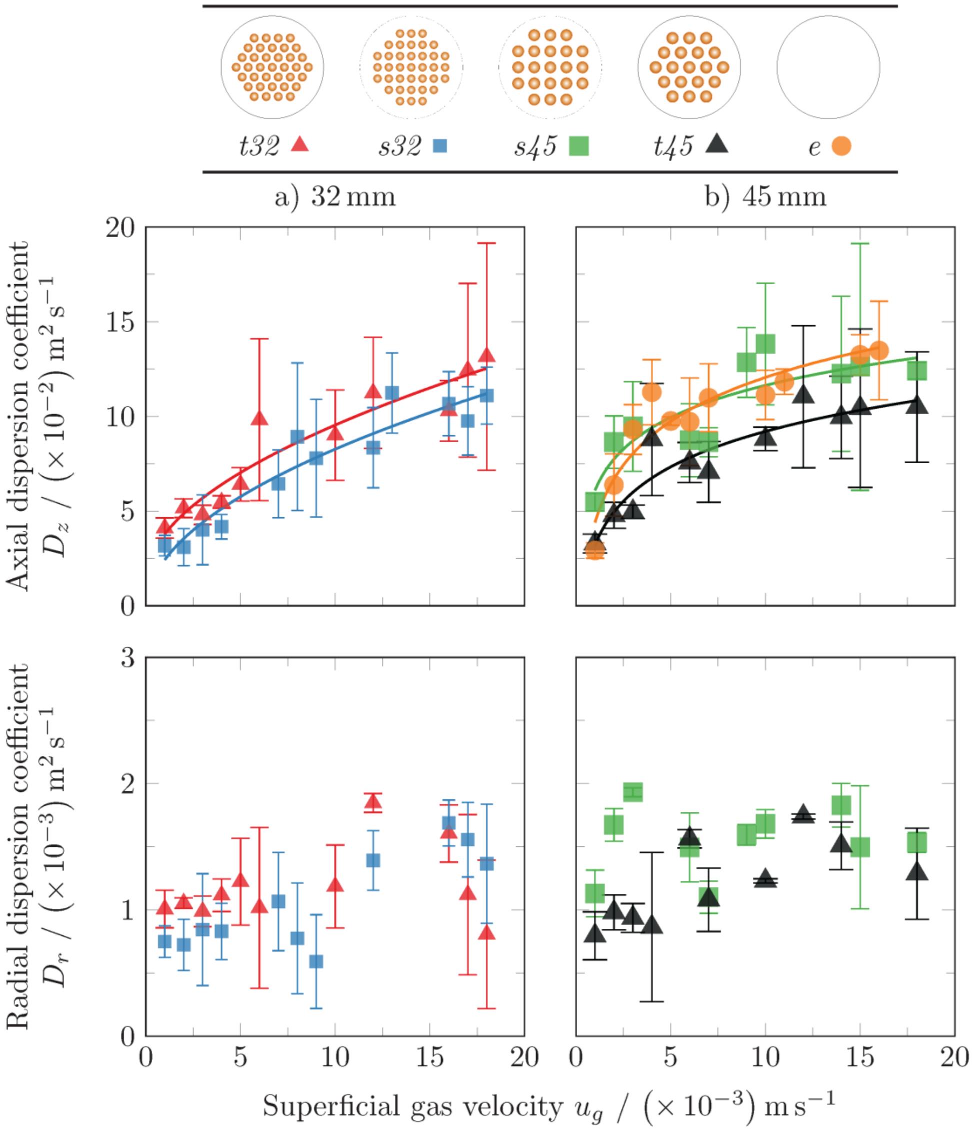

Figure 11: Axial (top row) and radial (bottom row) dispersion coefficient as a function of the superficial gas velocity for internals with a) 32 mm tubes and b) 45 mm tubes as well as empty column.

The error bars indicate the standard deviation from three repeated measurements, i.e. three measurements per configuration and flow rate, which increases at churn-turbulent conditions. The axial dispersion coefficient increases with increasing superficial gas velocity, which is in line with the literature (Baird and Rao, 1998; Baird and Rice, 1975; Deckwer et al., 1974; Rubio et al., 2004). For the smaller tube configurations (*s32*, *t32*), the axial dispersion coefficient is continuously increasing, while the coefficient levels off in the heterogeneous flow regime for the larger tubes and the empty column. This phenomenon can be described by the formation of large liquid circulation cells for smaller tubes and sub-channels, which enhances the liquid mixing.

The radial dispersion coefficients (Figure 11, lower row) obtained from the 2D dispersion model via Equation 9 are very low and nearly constant ($1\times10^{-3}\,m^2\,s^{-1}$) regardless of operating conditions and internals, which again confirms the radial flow exchange suppression caused by the funneling effect and the formation of Taylor-bubbles.

The mixing time, which is presented as a function of the superficial gas velocity in Figure 12, is reached at $c_t = 0.95$. In the case of a concentration overshoot the mixing time is reached at $c_t = 1.05$.

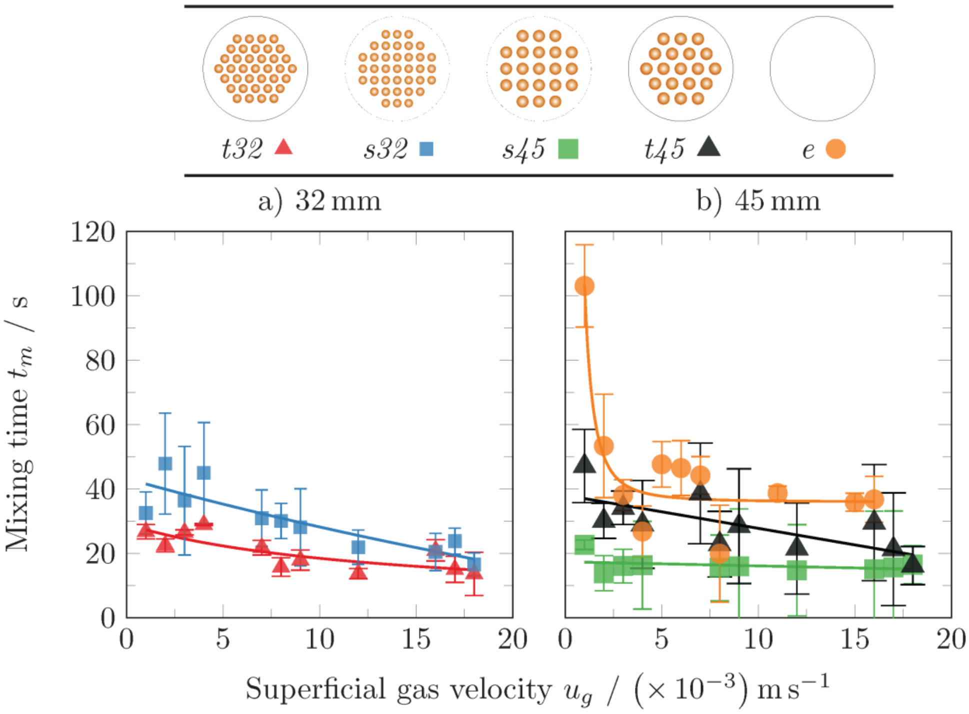

Figure 12: Mixing time as a function of the superficial gas velocity for internals with a) 32 mm tubes and b) 45 mm tubes as well as empty column.

With increasing superficial gas velocity the mixing time decreases for all configurations. The internals promote the mixing via formed larger liquid circulation cells. The fastest mixing time is obtained for the Square 45 (*s45*) configuration, where the large sub-channels feature large bubbles, which, in turn, have a higher momentum. Bernemann (1989) stated that tube configurations, which promote coalescence, feature steeper liquid velocity gradients and, hence, a faster liquid mixing. This also holds for the Square 45 (*s45*) configuration. For the small-tubes configurations, on the other hand, a different effect governs the high mixing time, namely, the formation of larger liquid circulation cells (as already discussed above). These findings are also in line with the previous study in a narrow column (Lau et al., 2018; Möller et al., 2018a).

4.3.2 Gas-liquid mass transfer

The volumetric mass transfer coefficient and the liquid-side mass transfer coefficient are displayed as a function of the superficial gas velocity in Figure 13. Again, the error bars indicate the standard deviation from three repeated measurements.

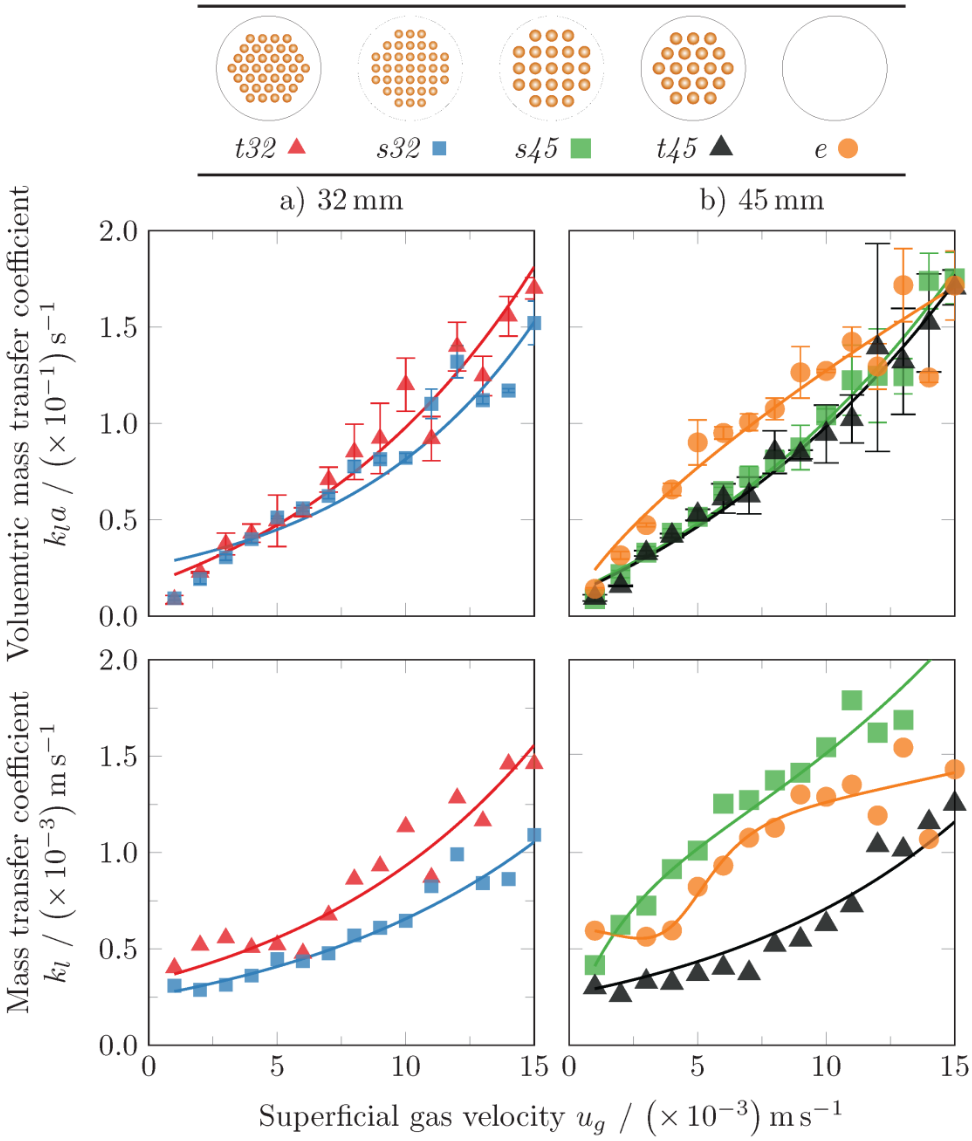

Figure 13: Volumetric mass transfer coefficient (top row) and liquid-side mass transfer coefficient (bottom row) as a function of the superficial gas velocity for a) 32 mm and b) 45 mm tubes.

The volumetric mass transfer coefficients were determined using the axial dispersion model and the correlation of Wachi and Nojima (1990) for the gas dispersion coefficient. Hamed (2012) reported strongly decreasing axial gas dispersion coefficients when inserting internals, however, correlations for columns with internals are not available.

Figure 13 shows that the volumetric mass transfer coefficients increase with increasing superficial gas velocity for all configurations. The values are in a similar range compared to the empty BCR since the competing effects of higher turbulence levels (empty column) and higher gas holdup (columns with internals) counterbalance each other. These findings are consistent with the literature on larger column diameters (Hamed, 2012) and narrow columns (Möller et al., 2018b).

The liquid-side mass transfer coefficient (see Figure 13, lower row), which was obtained considering the interfacial area (see Chapter 4.2.1), can be regarded as an indirect measure of turbulence. The turbulence level decreases with inserted internals due to the reduced radial fluid exchange (except for the Square 45 (*s45*) configuration with large sub-channels). It should be mentioned that these results are different from our previous measurements in the narrow column (0.1 m I.D.), where lower turbulence levels were obtained for inserted internals (Möller et al., 2018b), which is due to an increased tube spacing and a higher radial turbulence level for the pilot-scale column.

4.4 Correlating gas holdup, liquid dispersion coefficient and gas-liquid mass transfer coefficient

4.4.1 Gas holdup

The gas holdup is a critical design parameter and a reliable estimate of the influence of tube bundle layouts, sizes and column diameters are required. Berg (1993) studied BCRs with internals and proposed a correlation predicting their holdup data well. The correlation was derived according to

$$\varepsilon_\mathrm{g} = S, \qquad \frac{u_\mathrm{g}^3}{\nu_\mathrm{l} g} \frac{\rho_\mathrm{l}}{\rho_\mathrm{l} - \rho_\mathrm{g}} \leq 1, \tag{14}$$

$$\varepsilon_\mathrm{g} = \frac{S}{1 - S}, \qquad \frac{u_\mathrm{g}^3}{\nu_\mathrm{l} g} \frac{\rho_\mathrm{l}}{\rho_\mathrm{l} - \rho_\mathrm{g}} > 1, \tag{15}$$

where S is defined as

$$\mathrm{S} = C_1 (1 + C_2 K_\mathrm{h}) \left(\frac{u_\mathrm{g}^3}{\nu_\mathrm{l} g} \frac{\rho_\mathrm{l}}{\rho_\mathrm{l} - \rho_\mathrm{g}} \right)^{\mathrm{aFl^b}}, \tag{16}$$

where K_h is the coalescence factor (K_h = 0 for coalescing systems and K_h = 1 for non-coalescing systems). The dimensionless fluid number, Fl, is defined as

$$\mathrm{Fl} = \frac{\rho_\mathrm{l} \sigma^3}{g \eta_\mathrm{l}^4}. \tag{17}$$

As the research on BBRs with internals gained a big interest in the last years, the gas holdup database for these reactor types increased (Table 2). All these data are subsequently considered to derive an improved gas holdup correlation, which considers the internals' geometry. The abbreviations, c, t and s represent the configurations' patterns, namely circular, triangular, and square.

Table 2: Experimental database considered to derive an improved gas holdup correlation.

Author	**ID**	D	n	d_0	**Pattern**	A_c	A/V	u_g
	-	m	-	m	-	%	m^{-1}	$(\times 10^{-3})$ $m\,s^{-1}$
Youssef (2010)	YC15	0.44	30	0.025	c	15	25	5-45
	YT20		66		t	20	44	
	YT25		75		t	25	48	
	YC5	0.19	12	0.013	c	5	38	3-20
	YT22		48		t	22	89	
Bernemann (1989)	BT11	0.45	13	0.025	t	11	15	1-44
Guan et al. (2015)	GT9	0.8	83	0.025	t	9	18	8-62
Kagumba (2013)	KT25	0.14	30	0.013	t	25	106	3-45
Mesfer et al. (2016)	AT25	0.14	30	0.013	t	25	106	7-45
Jhawar and Prakash (2014)	JC11	0.15	15	0.013	c	11	61	3-35
George (2015)	GC7	0.15	15	0.01	c	7	52	3-35
Hamed (2012)	HT22	0.19	4815	0.013	t	22	89	5-45
Jasim (2016)	JC25	0.14	30	0.013	c	25	106	2-45
	JT25				t			
Möller et al. (2018b)	MS22	0.1	13	0.013	s	22	108	2-20
	MS24		37	0.08	s	24	158	
	MT24		37	0.08	t	24	158	
	MT22		13	0.013	t	22	108	
This work	MS25	0.392	37	0.032	s	25	41	1-15
	MT25		37	0.032	t	25	41	
	MT252		19	0.045	t	25	32	

Berg (1993) incorporated the internals' effect by the effective gas velocity, which is the superficial gas velocity based on the free area. However, geometrical details of the various internals were not considered. Thus, a dimensionless geometry factor, G, to properly account for the crucial tube bundle design parameters (occlusion area, A_c, column diameter, D, number of tubes, N, tube diameter, d_o, and volumetric heat exchanger area, A/V) is proposed based on a parameter analysis resulting in

$$G = A_\mathrm{c}(DNd_\mathrm{o})\left(\frac{A}{V}\right)^2 . \tag{18}$$

Accordingly, the correlation of Berg (1993) is modified to

$$\mathrm{S} = \mathrm{C}_1(1 + \mathrm{C}_2 K_\mathrm{h})\left(\frac{u_\mathrm{g}^3}{\nu_\mathrm{l}\mathrm{g}}\frac{\rho_\mathrm{l}}{\rho_\mathrm{l} - \rho_\mathrm{g}}\right)^{\mathrm{aFl}^\mathrm{b}} G^\mathrm{c}. \tag{19}$$

The fitting coefficients in Equation 19 (C_1, a, b) were determined applying the least square method (Table 3). Since the liquid properties were not modified in this article, C_2 is used as proposed by Berg (1993).

Table 3: Incorporation of the geometry factor using the correlation from Berg (1993).

Constants and conditions from Berg (1993)	**Constants and conditions new correlation**
$\frac{u_\mathrm{g}^3}{\nu_\mathrm{l}\mathrm{g}}\frac{\rho_\mathrm{l}}{\rho_\mathrm{l}-\rho_\mathrm{g}} \leq 1$ bubble swarm region,	$\frac{u_\mathrm{g}^3}{\nu_\mathrm{l}\mathrm{g}}\frac{\rho_\mathrm{l}}{\rho_\mathrm{l}-\rho_\mathrm{g}} \leq 2$bubble swarm region,
$\frac{u_\mathrm{g}^3}{\nu_\mathrm{l}\mathrm{g}}\frac{\rho_\mathrm{l}}{\rho_\mathrm{l}-\rho_\mathrm{g}} > 1$ bubble train region,	$\frac{u_\mathrm{g}^3}{\nu_\mathrm{l}\mathrm{g}}\frac{\rho_\mathrm{l}}{\rho_\mathrm{l}-\rho_\mathrm{g}} > 2$ bubble train region,
$\mathrm{C}_1 = 0.1$ bubble swarm region,	$\mathrm{C}_1 = 0.16$ bubble swarm region,
$\mathrm{C}_1 = 0.11$ bubble train region,	$\mathrm{C}_1 = 0.25$ bubble train region,
$\mathrm{C}_2 = 0.93$,	$\mathrm{C}_2 = 0.93$,
$\mathrm{a} = 0.3$, $\mathrm{b} = -0.018$	$\mathrm{a} = 1.63, \mathrm{b} = -0.067, \mathrm{c} = -0.021$

In Figure 14 the prediction from the new correlation is validated against the measurement data from literature and from this work (Table 2). It should be noted that the bubble train and swarm region shift to larger values (see Table 3), which is due to the prolonged homogeneous flow regime for columns with internals as discussed earlier (see Figure 5).

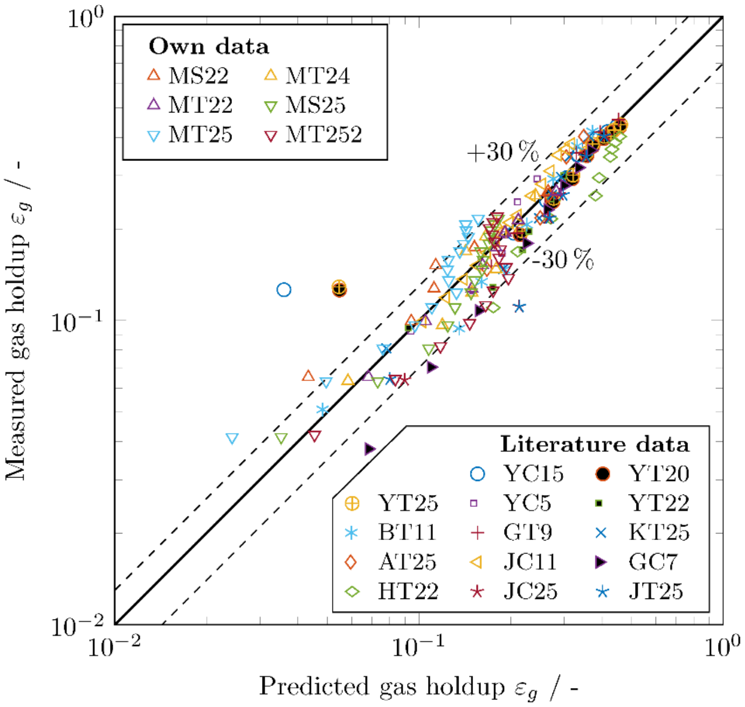

Figure 14: Evaluation of the developed holdup correlation containing a geometry factor to consider the various patterns with experimental and literature data.

The developed correlation describes the measurement data fairly well as shown by the error lines (except for the data from YC15, YT20 and YT24, where the experimental gas holdup data are exceptionally high). The correlation is able to predict different tube patterns (square, triangular, circular) with several tube sizes (8×10^{-3} m to 45×10^{-2} m), column diameters (0.1 m to 0.8 m) and various volumetric heat exchanger areas (15 m^{-1} to 157 m^{-1}) with a confidence interval of approximately 30% and an AARE of circa 16%. It should be noted that the current correlation was only developed for water/air bubble columns since data from different systems are very rare.

4.4.2 Axial dispersion coefficient

So far, the effect of internals has not been considered in correlations for the axial dispersion coefficient. Baird and Rice (1975) proposed a correlation for the liquid dispersion coefficient based on a semi-theoretical approach for empty BCRs according to

$$D_\mathrm{z} = 0.35\left(g u_\mathrm{g}\right)^{0.33} D^{1.33}. \tag{20}$$

To consider the effect of internals in Equation 20, a modification is proposed based on own experimental data for a narrow column (Möller et al., 2018a, 2018b) and from the pilot-scale column determined in this study. Therefore, the correlation from Baird and Rice (1975) is modified considering the decisive parameters (tube diameter, pattern and cross-sectional area occlusion) according to

$$D_{\mathrm{z}} = 14.06^{\sin(-1.52\,\theta)}\left(g u_{\mathrm{g}}\right)^{0.47} D^{1.21}\left(1-A_{\mathrm{c}}\right)^{-5.76}\left(\frac{A_{\mathrm{s}}}{d_{\mathrm{h}}^{2}}\right)^{-5.7}. \tag{21}$$

Here, $\sin(\theta)$ represents the pattern with θ = 60° for triangular configurations and θ = 90° for square configurations, respectively. In Figure 15, the prediction of the new correlation is validated against the experimental data (note that the abbreviations are according to Table 2).

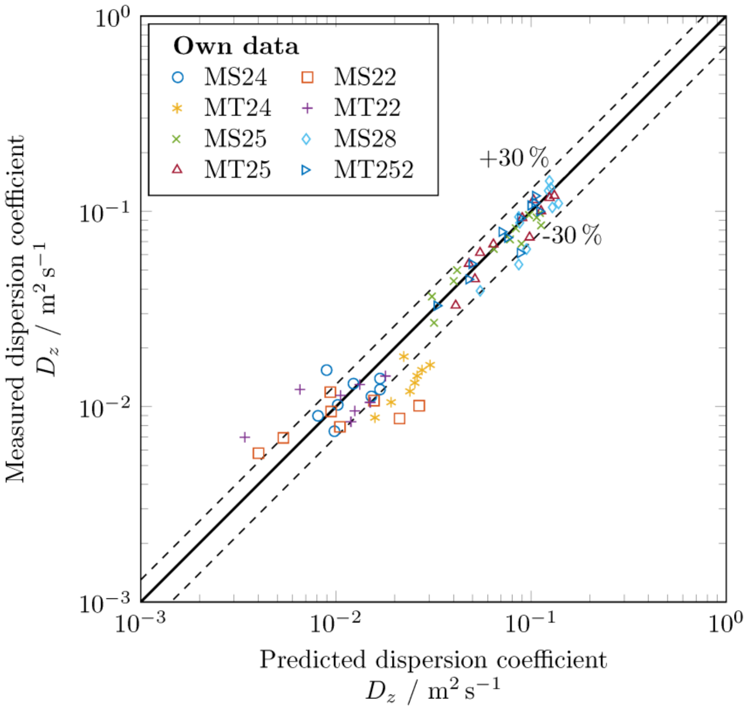

Figure 15: Evaluation of the developed dispersion coefficient correlation containing a geometry factor to consider the various patterns with experimental and literature data.

The correlation predicts triangular and square patterns with a tube size of 8×10^{-3} m to 45×10^{-3} m in columns with diameters of 0.1 m to 0.392 m and volumetric heat transfer areas from 15 m^{-1} to 157 m^{-1} well. However, the prediction for the triangular configuration with 8×10^{-3} m (MT24) tubes deviates due to the formation of larger circulation cells.

4.4.3 Volumetric mass transfer

Eventually, the volumetric mass transfer coefficient for columns with internals is also correlated using the mass transfer data from Möller et al. (2018b) and this study. The correlation developed by Akita and Yoshida (1973), derived from a dimension analysis for empty BCRs, according to

$$k_{\mathrm{l}}a\frac{D}{D_{\mathrm{l}}} = 0.6\mathrm{Sc}^{0.5}\mathrm{Bo}^{0.82}\mathrm{Ga}^{0.31}\varepsilon_{\mathrm{g}}^{1.1} \tag{22}$$

was used as the starting point. Since the mass transfer coefficient depends not only on the gas holdup but also on the superficial gas velocity, the correlation was extended by the dimensionless Froude number. Furthermore, geometrical terms are considered to account for the tube bundles according to

$$k_{\mathrm{l}}a\frac{D}{D_{\mathrm{l}}} = 18.34^{\sin(-2.67\theta)}\mathrm{Sc}^{0.5}\mathrm{Bo}^{2.86}\mathrm{Ga}^{-0.96}\varepsilon_{\mathrm{g}}^{0.41}\mathrm{Fr}^{0.32}(1-A_{\mathrm{c}})^{7.41}\left(\frac{A_{\mathrm{s}}}{d_{\mathrm{h}}^{2}}\right)^{-18.79}, \tag{23}$$

where

$$\mathrm{Sc} = \frac{\nu_{\mathrm{l}}}{D_{\mathrm{l}}}, \mathrm{Bo} = \frac{gD^{2}\rho_{\mathrm{l}}}{\sigma}, \mathrm{Ga} = \frac{gD^{3}}{\nu_{\mathrm{l}}}, \mathrm{Fr} = \frac{u_{\mathrm{g}}^{2}}{gD} \ . \tag{24}$$

Predictions and measurement data agree fairly well (Figure 16).

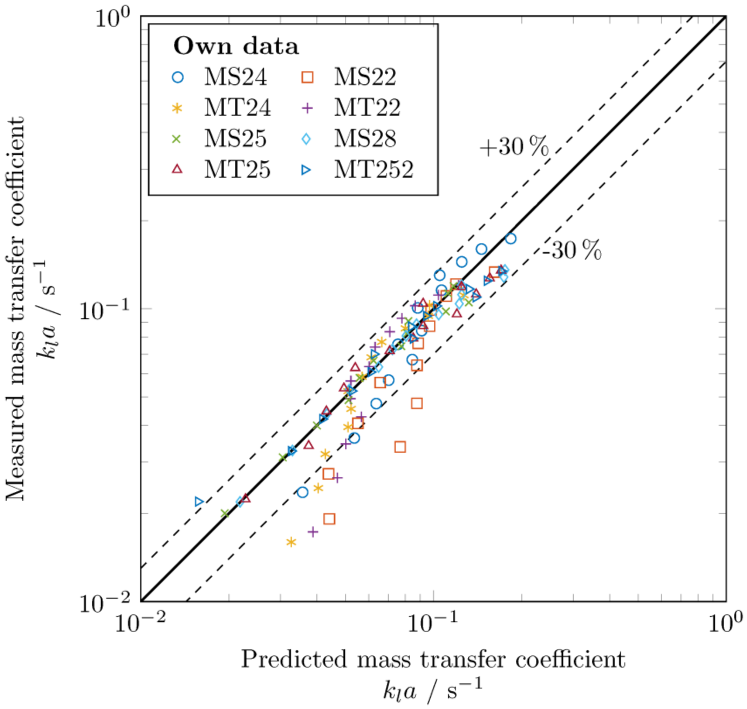

Figure 16: Evaluation of the developed mass transfer coefficient correlation containing a geometry factor to consider the various patterns with experimental and literature data.

5 Conclusion

In this article, cross-sectional and sub-channel gas-phase dynamics, liquid mixing and gas-liquid mass transfer have been comprehensively studied. A customized three-layered wire-mesh sensor and fastresponding oxygen needle probes were applied. The effect of column diameter, tube layout and tube size on flow regime boundaries have been identified. The results can be summarized as follows:

- Internals prolong the homogenous flow regime due to an increased bubble breakup frequency. Furthermore, the interaction of increasing column diameter and square configuration extend the regime transition, whereas triangular patterns decrease the regime transition velocity with increasing column diameter.
- The mixing time in columns with internals decreases significantly due the creation of larger liquid circulation cells. Furthermore, structures which facilitate coalescence, e.g. large sub-channels for the Square 45 (*s45*) configuration, provide steeper liquid velocity profile gradients and further promote the liquid mixing.
- Comparing results from narrow and pilot-scale columns, it can be concluded that internals decrease the volumetric mass transfer, provoke flow asymmetries and increase the bubble breakup frequency. Furthermore, the sub-channel layout has a strong influence on the flow dynamics.
- The wall in narrow columns stabilizes the flow, which was not observed for larger columns. The sub-channel wall even stabilizes the formation of large Taylor-bubbles, which, in turn, decreases holdup and increases the Sauter mean bubble diameter contrary to narrow columns.
- New correlations for gas holdup, axial liquid dispersion coefficient and volumetric mass transfer coefficient were proposed, which consider column scale, tube pattern and tube size.

Nomenclature

Abbreviations

BCR	Bubble column reactor
CSA	Cross-sectional area
KE	Kolmogorov entropy, bits s^{-1}
PDF	Probability density function
WMS	Wire-mesh sensor

Symbols

A/V	Volumetric heat transfer area, m^{-1}
A_c	Coverage of the cross-sectional area, %
A_p	Pixel area, m^2
A_s	Sub-channel area, m^2
$A_\mathrm{t,f}$	Total free pixel area, m^2
a	Interfacial area, m^{-1}

$a_{i,j}$	Weighting factor, -
c^*	Equilibrium concentration, mol m^{-3}
c_i	Gas or liquid phase concentration, mol m^{-3}
c_T	Dimensionless tracer concentration or mixing scalar, -
D	Column diameter, m
D_l	Liquid diffusivity coefficient, m^2 s^{-1}
$D_\mathrm{r,l}$	Radial liquid dispersion coefficient, m^2 s^{-1}
$D_{\mathrm{z},i}$	Axial dispersion coefficient for gas or liquid phase, m^2 s^{-1}
d_{32}	Sauter mean diameter, m
d_e	Equivalent diameter, m
d_h	Hydraulic sub-channel diameter, m
d_o	Outer tube diameter, m
Fl	Fluid number, -
G	Dimensionless geometrical constant, -
g	Earth acceleration, m s^{-2}
H	Henry constant, -
J_o	Zero order Bessel function, -
K_s	Sensor constant, -
K_h	Coalescence factor, -
k_l	Liquid-side mass transfer coefficient, m s^{-1}
$k_\mathrm{l}a$	Volumetric mass transfer coefficient, s^{-1}
k_max	Number of measurement frames, -
L_i	Dynamic (d) or static (s) liquid height, m
l_v	Voxel edge length, m
N	Number of tubes, -
N_v	Number of valid pixels within the WMS cross-section, -
n_b	Number of voxels, -
P	Tube pitch, m
R	Column radius, m
R^*	Dimensionless radius for the 2D-dispersion model, -
r	Radial position along the column radius, m
r^*	Dimensionless radial position, -
r/R	Dimensionless radius, -
t	Time, s
t^*	Dimensionless time, -
t_m	Mixing time, s

$U_{m,i,j,k}$	WMS digital, cross-sectional and temporal conductivity value, -
$U_{w,i,j}$	WMS digital and cross-sectional water conductivity value, -
u_g	Superficial gas velocity, $\mathrm{m\,s^{-1}}$
V_b	Bubble volume, $\mathrm{m^3}$
v_b	Bubble rise velocity, $\mathrm{m\,s^{-1}}$

Greek symbols

Δt	Time difference, s
η_l	Dynamic liquid viscosity, Pa s
ε_g	Total gas holdup, -
ν_l	Kinematic liquid viscosity, $\mathrm{m^2\,s^{-1}}$
ν_m	The *m*th root of the first-order Bessel function
ρ_i	Liquid or liquid density, $\mathrm{kg\,m^{-3}}$
σ	Surface tension, $\mathrm{Nm^{-1}}$

References

Akita, K., Yoshida, F., 1973. Gas Holdup and Volumetric Mass Transfer Coefficient in Bubble Columns. Effects of Liquid Properties. Industrial & Engineering Chemistry Process Design and Development 12, 76–80.

Baird, M.H.I., Rao, N.V.R., 1998. Axial mixing in a 15 cm diameter reciprocating plate bubble column. The Canadian Journal of Chemical Engineering 76, 370–378.

Baird, M.H.I., Rice, R.G., 1975. Axial dispersion in large unbaffled columns. The Chemical Engineering Journal 9, 171–174.

Berg, S., 1993. Zur Gasgehaltsverteilung und zum Verweilzeitverhalten der Gasphase in Blasensäulen mit längsangeströmten Rohrbündeleinbauten. TU Dortmund.

Bernemann, K., 1989. Zur Fluiddynamik und zum Vermischungsverhalten der flüssigen Phasen in Blasensäulen mit längsangeströmten Rohrbündeln. TU Dortmund.

Besagni, G., Gallazzini, L., Inzoli, F., 2017. On the scale-up criteria for bubble columns. Petroleum.

Beyer, M., Szalinski, L., Schleicher, E., Schunk, C., 2018. Wire-mesh Sensor Data Processing Software. HZDR Innovation. http://mpmt.de/de/produkte/gittersensor/de/downloads/wire-mesh-sensor-data-processing-software. December, 3, 2018.

Bhusare, V.H., Dhiman, M.K., Kalaga, D.V., Roy, S., Joshi, J.B., 2017. CFD simulations of a bubble column with and without internals by using OpenFOAM. Chemical Engineering Journal 317, 157–174.

Deckwer, W.D., 1992. Bubble Column Reactors. John Wiley & Sons Inc.

Deckwer, W.-D., Adler, I., Zaidi, A., 1978. A comprehensive study on CO2-interphase mass transfer in vertical cocurrent and countercurrent gas-liquid flow. The Canadian Journal of Chemical Engineering 56, 43–55.

Deckwer, W.-D., Burckhart, R., Zoll, G., 1974. Mixing and mass transfer in tall bubble columns. Chemical Engineering Science 29, 2177–2188.

Deckwer, W.-D., Schumpe, A., 1993. Improved tools for bubble column reactor design and scale-up. Chemical Engineering Science 48, 889–911.

Döß, A., Schubert, M., Bieberle, A., Hampel, U., 2017. Non-invasive determination of gas phase dispersion coefficients in bubble columns using periodic gas flow modulation. Chemical Engineering Science 171, 256–270.

Forret, A., Schweitzer, J.-M., Gauthier, T., Krishna, R., Schweich, D., 2003. Liquid Dispersion in Large Diameter Bubble Columns, with and without Internals. The Canadian Journal of Chemical Engineering 81, 360–366.

Furuya, M., Kanai, T., Arai, T., Takiguchi, H., Prasser, H.-M., Hampel, U., Schleicher, E., 2017. Three-dimensional velocity vector determination algorithm for individual bubble identified with Wire-Mesh Sensors. Nuclear Engineering and Design.

George, K.J.H., 2015. Investigations in Hydrodynamics and Mixing Pattern in the Bubble Column Equipped with Internals. The University of Western Ontario.

Guan, X., Gao, Y., Tian, Z., Wang, L., Cheng, Y., Li, X., 2015. Hydrodynamics in bubble columns with pin-fin tube internals. Chemical Engineering Research and Design 102, 196–206.

Guan, X., Li, Z., Wang, L., Cheng, Y., Li, X., 2014. CFD Simulation of Bubble Dynamics in Bubble Columns with Internals. Industrial and Engineering Chemistry Research 53, 16529–16538.

Guan, X., Yang, N., 2017. CFD simulation of pilot-scale bubble columns with internals: Influence of interfacial forces. Chemical Engineering Research and Design 126, 109–122.

Guo, X., Chen, C., 2017. Simulating the impacts of internals on gas–liquid hydrodynamics of bubble column. Chemical Engineering Science 174, 311–325.

Hamed, M., 2012. Hydrodynamics Mixing and Mass Transfer in Bubble Columns with Internals. Washington University St. Louis.

Han, L., Al-Dahhan, M.H., 2007. Gas-liquid mass transfer in a high pressure bubble column reactor with different sparger designs. Chemical Engineering Science 62, 131–139.

HZDR Innovation, -, 2013. ClockBox V5 / ClockControl V3. HZDR Innovation. http://mpmt.de/de/produkte/clock-box?set_language=de.

Jasim, A., 2016. The impact of heat exchanging internals on hydrodynamics of bubble column reactor. Missouri University of Science and Technology.

Jhawar, A.K., Prakash, A., 2014. Bubble column with internals: Effects on hydrodynamics and local heat transfer. Chemical Engineering Research and Design 92, 25–33.

Kagumba, M.O.O., 2013. Heat transfer and Bubble Dynamics in Bubble and slurry Bubble column with internals for Fischer-Tropsch synthesis of clean alternative fuels and chemicals. Missouri University of Science and technology.

Kalaga, D.V., Bhusare, V., Pant, H.J., Joshi, J.B., Roy, S., 2018. Impact of Dense Internals on Fluid Dynamic Parameters in Bubble Column. International Journal of Chemical Reactor Engineering 0.

Kalaga, D.V., Y., A., Goswami, S., Bhusare, V., Pant, H.J., Dalvi, S.V., Joshi, J.B., Roy, S., 2017. Comparative analysis of liquid hydrodynamics in a co-current flow-through bubble column with densely packed internals via radiotracing and Radioactive Particle Tracking (RPT). Chemical Engineering Science 170, 332–346.

Kipping, R., Brito, R., E.Scheicher, Hampel, U., 2016. Developments for the application of the Wire-Mesh Sensor in industries. International Journal of Multiphase Flow 85, 86–95.

Kipping, R., Kryk, H., Schleicher, E., Gustke, M., Hampel, U., 2017. Application of a wire-mesh sensor for the study of chemical species conversion in a bubble column. Chemical Engineering & Technology 40, 1425–1433.

Laborde-Boutet, C., Larachi, F., Dromard, N., Delsart, O., Béliard, P.-E., Schweich, D., 2010. CFD simulations of hydrodynamic/thermal coupling phenomena in a bubble column with internals. AIChE Journal 56, 2397–2411.

Larachi, F., Desvigne, D., Donnat, L., Schweich, D., 2006. Simulating the effects of liquid circulation in bubble columns with internals. Chemical Engineering Science 61, 4195–4206.

Lau, Y.M., Möller, F., Hampel, U., Schubert, M., 2018. Ultrafast X-ray tomographic imaging of multiphase flow in bubble columns – Part 2: Characterisation of bubbles in the dense regime. International Journal of Multiphase Flow.

Li, H., Prakash, A., 2001. Survey of heat transfer mechanisms in a slurry bubble column. The Canadian Journal of Chemical Engineering 79, 717–725.

Mesfer, M.K.A., Sultan, A.J., Al-Dahhan, M.H., 2016. Impacts of dense heat exchanging internals on gas holdup cross-sectional distributions and profiles of bubble column using gamma ray Computed Tomography (CT) for FT synthesis. Chemical Engineering Journal 300, 317–333.

Mesfer, M.K.A., Sultan, A.J., Al-Dahhan, M.H., 2017. Study the effect of dense internals on the liquid velocity field and turbulent parameters in bubble column for Fischer–Tropsch (FT) synthesis by using Radioactive Particle Tracking (RPT) technique. Chem. Eng. Sci. 161, 228–248.

Möller, F., Lau, Y.M., Seiler, T., Hampel, U., Schubert, M., 2018a. A study on the influence of the tube layout on sub-channel hydrodynamics in a bubble column with internals. Chemical Engineering Science 179, 265–283.

Möller, F., MacIsaac, A., Lau, Y.M., Schleicher, E., Hampel, U., Schubert, M., 2018b. Advanced Analysis of Liquid Dispersion and Gas-Liquid Mass Transfer in a Bubble Column with Dense Vertical Internals. Chemical Engineering Research and Design.

Nedeltchev, S., 2009. Application of Chaos Analysis for the Investigation of Turbulence in Heterogeneous Bubble Columns. Chemical Engineering & Technology 32, 1974–1983.

Nedeltchev, S., Donath, T., Rabha, S.S., Hampel, U., Schubert, M., 2014. New Evidence for the Mixing Length Concept in a Narrow Bubble Column Operated in the Transition Regime. Journal of Chemical Engineering of Japan 47, 722–729.

Nedeltchev, S., Möller, F., Hampel, U., Schubert, M., 2018. Flow Regime Transitions in a Bubble Column with Internals Based On a Novel Approach. Chemical Engineering Journal Japan.

Nedeltchev, S., Möller, F., Schubert, M., 2017. Effect of Heat Exchanger Internals on the Main Transition Velocities in a Bubble Column. In: Proceeding Third International SymposiumMultiscaleMultiphaseProcessEngineering(MMPE).

Nedeltchev, S., Shaikh, A., 2013. A new method for identification of the main transition velocities in multiphase reactors based on information entropy theory. Chemical Engineering Science 100, 2–14.

Ohki, Y., Inoue, H., 1970. Longitudinal mixing of the liquid phase in bubble columns. Chemical Engineering Science 25, 1–16.

Prasser, H.-M., Böttger, A., Zschau, J., 1998. A new electrode-mesh tomograph for gas-liquid flows. Flow Measurement and Instrumentation 9, 111–119.

Rollbusch, P., Bothe, M., Becker, M., Ludwig, M., Grünewald, M., Schlüter, M., Franke, R., 2015. Bubble columns operated under industrially relevant conditions – Current understanding of design parameters. Chemical Engineering Science 126, 660–678.

Rubio, F.C., Mirón, A.S., García, M.C.C., Camacho, F.G., Grima, E.M., Chisti, Y., 2004. Mixing in bubble columns: a new approach for characterizing dispersion coefficients. Chemical Engineering Science 59, 4369–4376.

Schlüter, S., 1992. Modellierung und Simulation von Blasensäulenreaktoren. na.

Schlüter, S., Steiff, A., Weinspach, P.-M., 1995. Heat transfer in two- and three-phase bubble column reactors with internals. Chemical Engineering and Processing: Process Intensification 34, 157–172.

Schouten, J.C., Takens, F., Bleek, C.M. van den, 1994. Maximum-likelihood estimation of the entropy of an attractor. Physical Review E 49, 126–129.

Shah, R.K., Sekulic, D.P., 2003. Fundamentals of Heat Exchanger Design. John Wiley & Sons.

Shah, Y.T., Kelkar, B.G., Godbole, S.P., Deckwer, W.-D., 1982. Design parameters estimations for bubble column reactors. AIChE Journal 28, 353–379.

Sharaf, S., Zednikova, M., Ruzicka, M.C., Azzopardi, B.J., 2016. Global and local hydrodynamics of bubble columns - Effect of gas distributor. Chemical Engineering Journal 288, 489–504.

Sultan, A.J., Sabri, L.S., Al-Dahhan, M.H., 2018a. Impact of Heat-Exchanging Tube Configurations on the Gas Holdup Distribution in Bubble Columns using Gamma-Ray Computed Tomography. International Journal of Multiphase Flow.

Sultan, A.J., Sabri, L.S., Al-Dahhan, M.H., 2018b. Influence of the size of heat exchanging internals on the gas holdup distribution in a bubble column using gamma-ray computed tomography. Chemical Engineering Science 186, 1–25.

Sultan, A.J., Sabri, L.S., Al-Dahhan, M.H., 2018c. Investigating the influence of the configuration of the bundle of heat exchanging tubes and column size on the gas holdup distributions in bubble columns via gamma-ray computed tomography. Experimental Thermal and Fluid Science 98, 68–85.

Thulukkanam, K., 2013. Heat Exchanger Design Handbook, 2nd Edition. ed. CRC Press.

Wachi, S., Nojima, Y., 1990. Gas-phase dispersion in bubble columns. Chemical Engineering Science 45, 901–905.

Westermeyer-Benz, H., 1992. Wärmeübergang und Gasgehalt in zwei-und dreiphasig betriebenen Blasensäulenreaktoren mit längseingebauten Rohren. TU Dortmund.

Wilkinson, P.M., Spek, A.P., Dierendonck, L.L. van, 1992. Design parameters estimation for scale-up of high-pressure bubble columns. AIChE Journal 38, 544–554.

Yamashita, F., 1987. Effects Of Vertical Pipe And Rod Internals On Gas Holdup In Bubble Columns. Journal of Chemical Engineering of Japan 20, 204–206.

Youssef, A.A., 2010. Fluid Dynamics and Scalue-Up of Bubble Columns with Internals. Washington University St. Louis.

Youssef, A.A., Al-Dahhan, M.H., 2009. Impact of Internals on the Gas Holdup and Bubble Properties of a Bubble Column. Industrial and Engineering Chemistry Research 48, 8007–8013.

Youssef, A.A., Al-Dahhan, M.H., Duduković, M.P., 2013. Bubble Columns with Internals: A Review. International Journal of Chemical Reactor Engineering 11, 169–223.

Youssef, A.A., Hamed, M.E., Al-Dahhan, M.H., Duduković, M.P., 2014. A new approach for scale-up of bubble column reactors. Chemical Engineering Research and Design 92, 1637–1646.

fig_1.png
Click here to download high resolution image

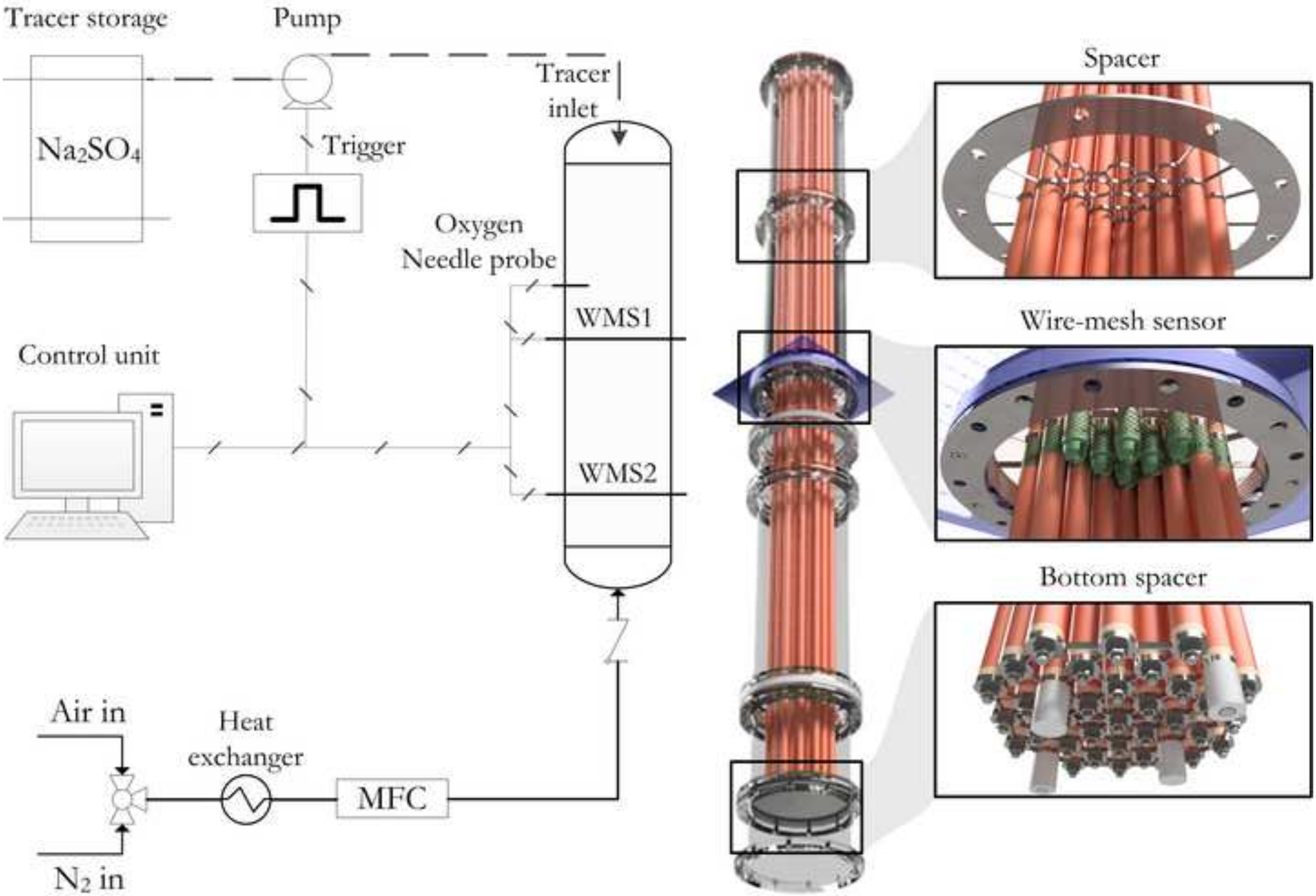
Tracer storage
Pump
Na$_2$SO$_4$
Tracer inlet
Trigger
Oxygen Needle probe
WMS1
Control unit
WMS2
Air in
Heat exchanger
MFC
N$_2$ in
Spacer
Wire-mesh sensor
Bottom spacer

fig_2.png

Click here to download high resolution image

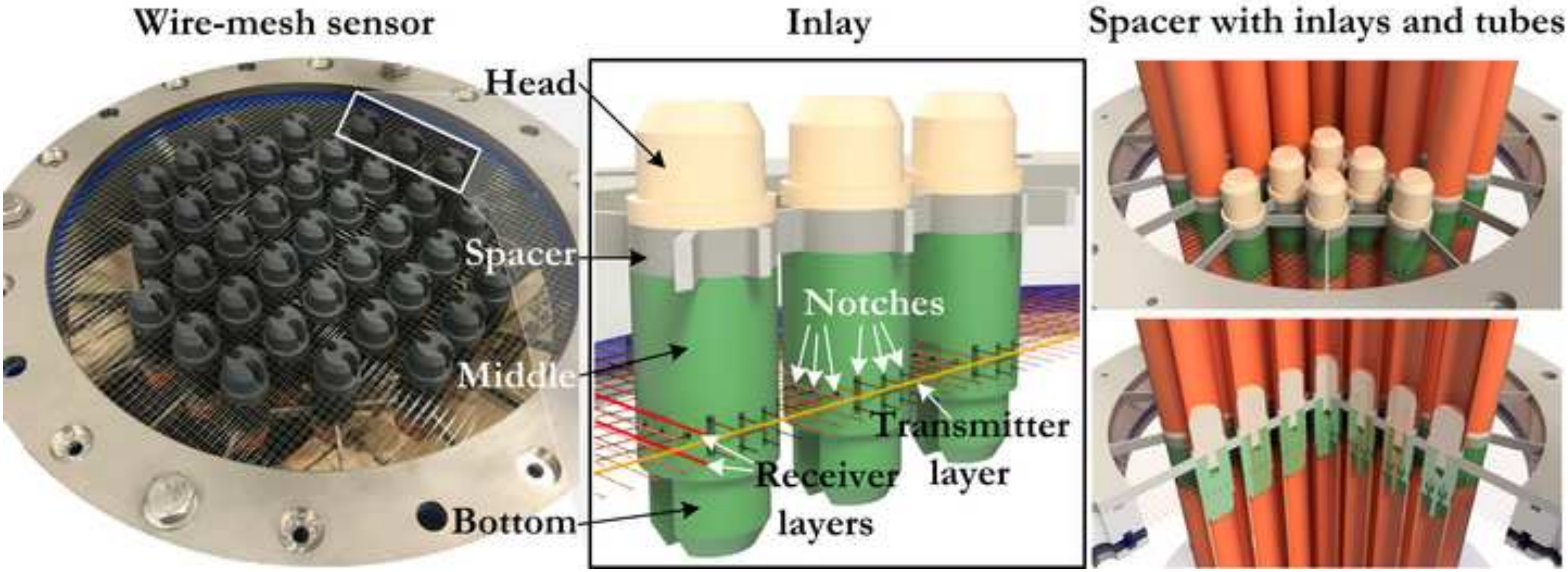
Wire-mesh sensor
Inlay
Spacer with inlays and tubes
Head
Spacer
Middle
Bottom
Notches
Transmitter layer
Receiver layers

fig_3.png
Click here to download high resolution image

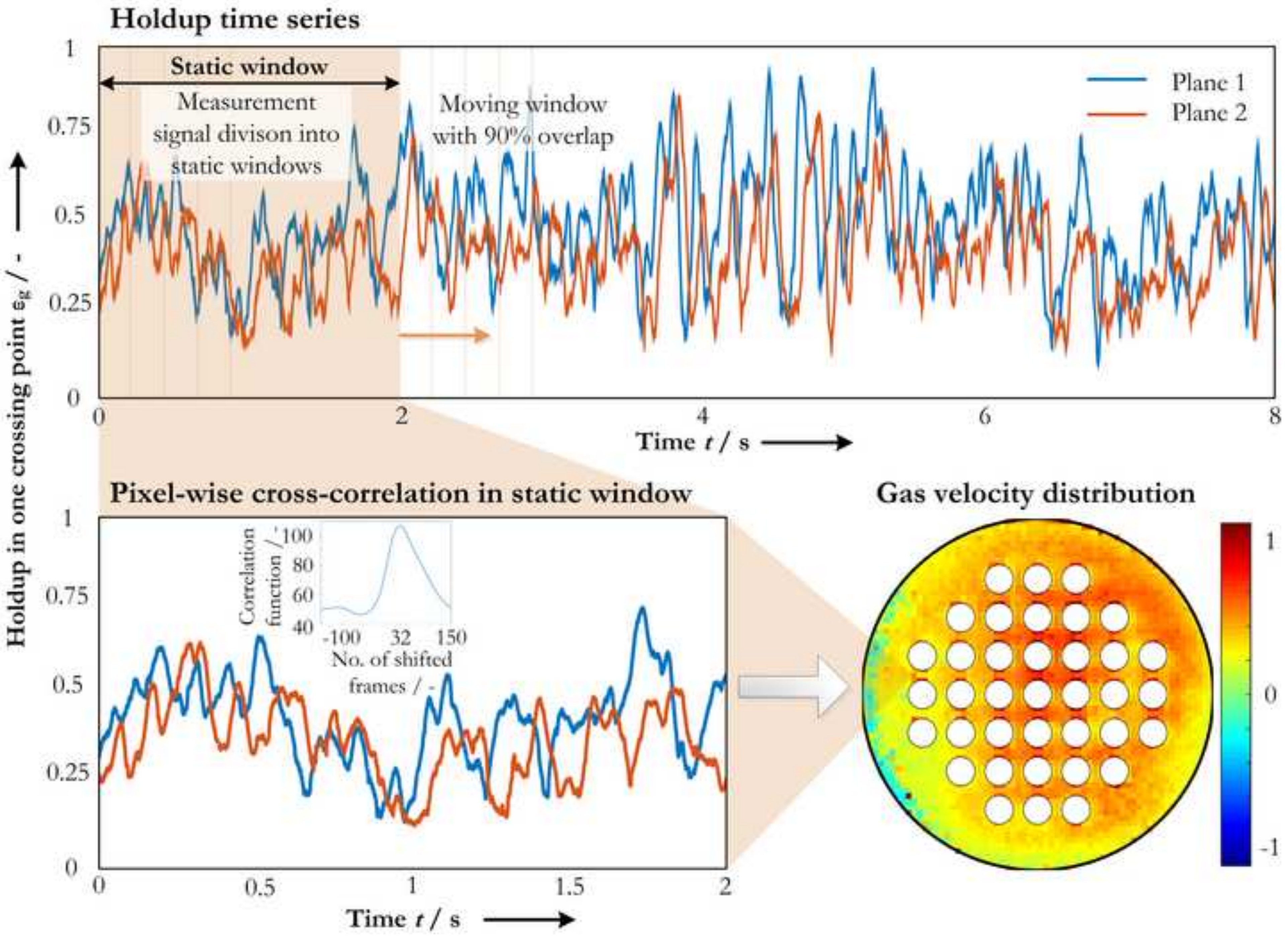

fig_4.pdf
Click here to download Figure: FIG_4.pdf

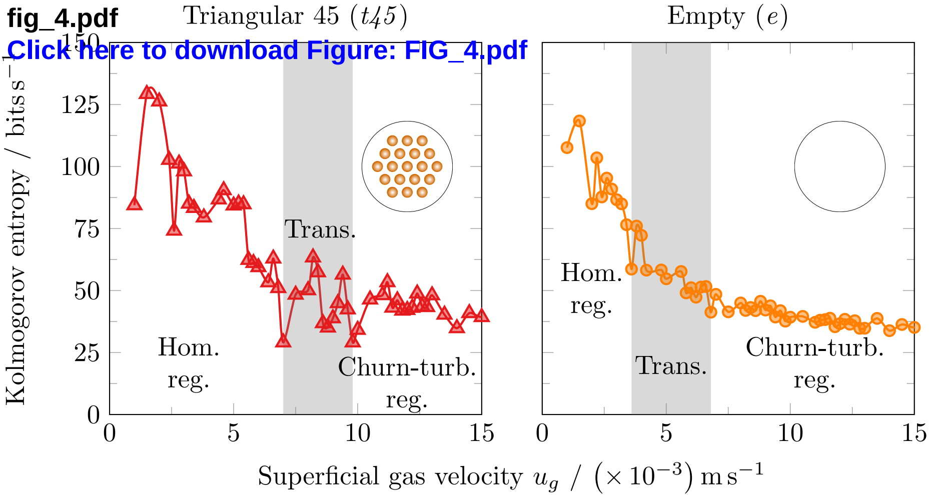

fig_5.pdf
Click here to download Figure: FIG_5.pdf

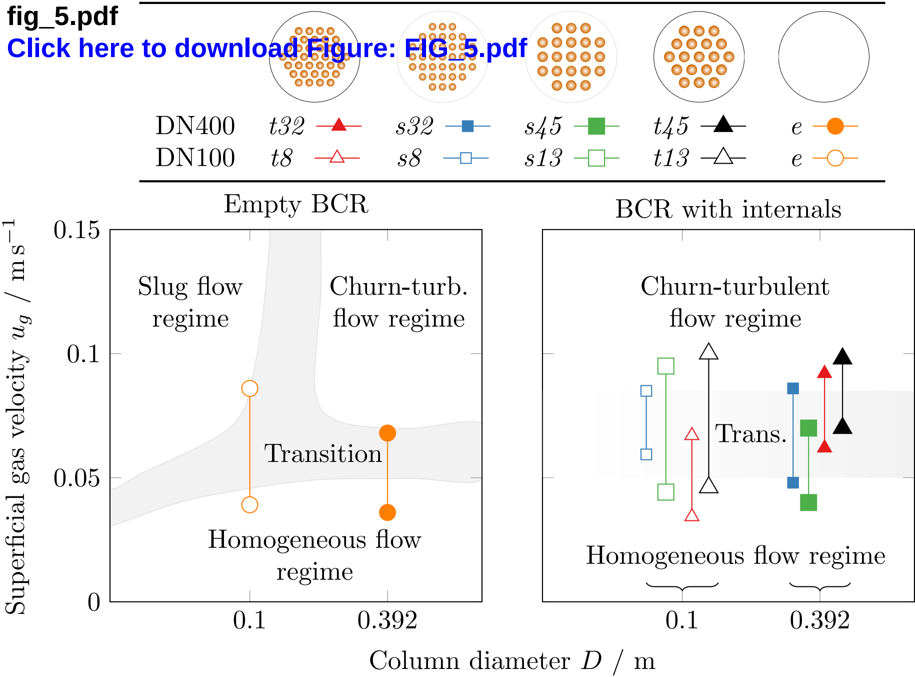

fig_6.pdf
Click here to download Figure: FIG_6.pdf

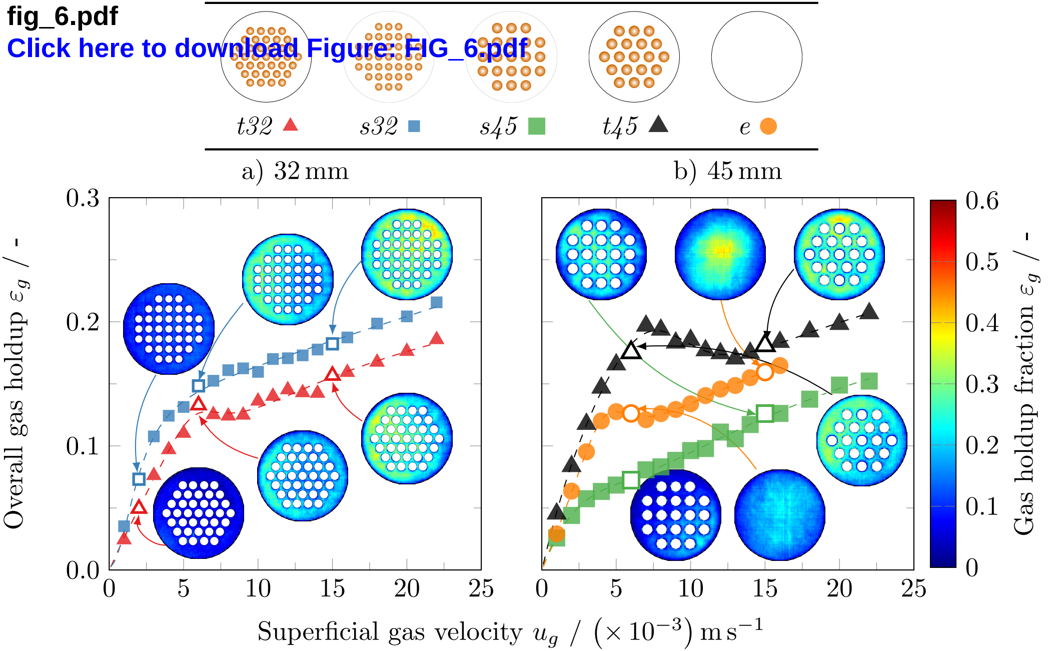

fig_7.pdf
Click here to download Figure: FIG_7.pdf

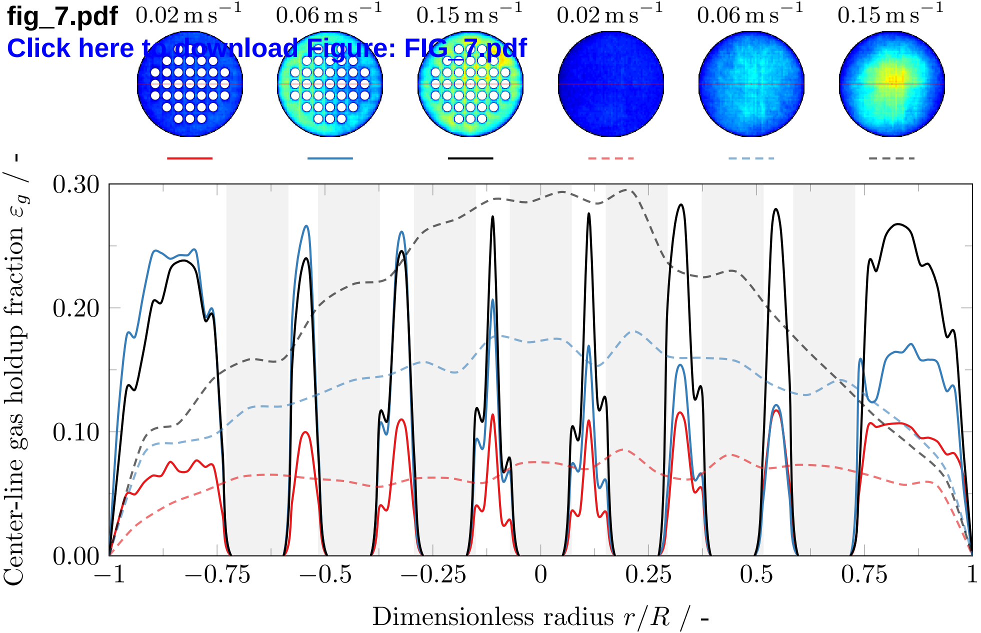

fig_8.pdf
Click here to download Figure: FIG_8.pdf

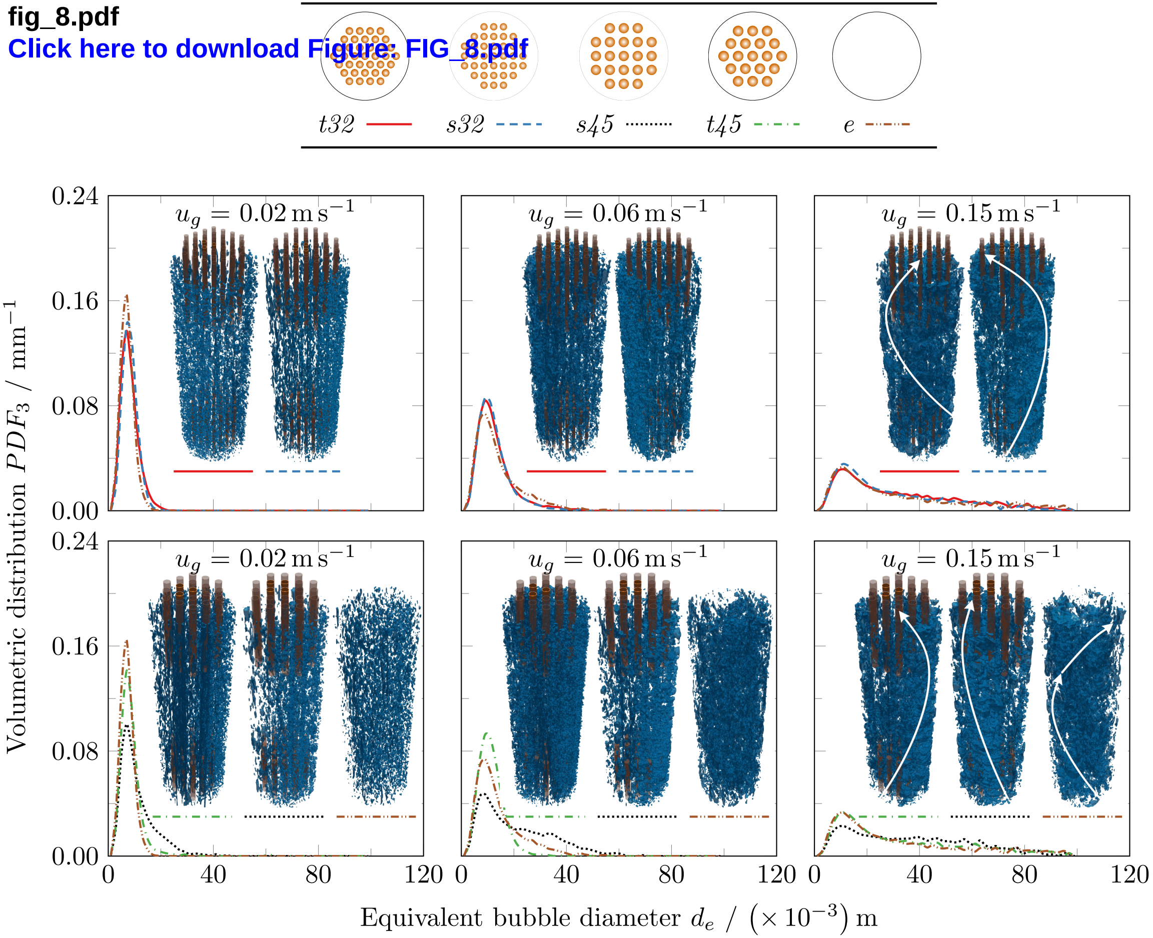

fig_9.pdf
Click here to download Figure: FIG_9.pdf

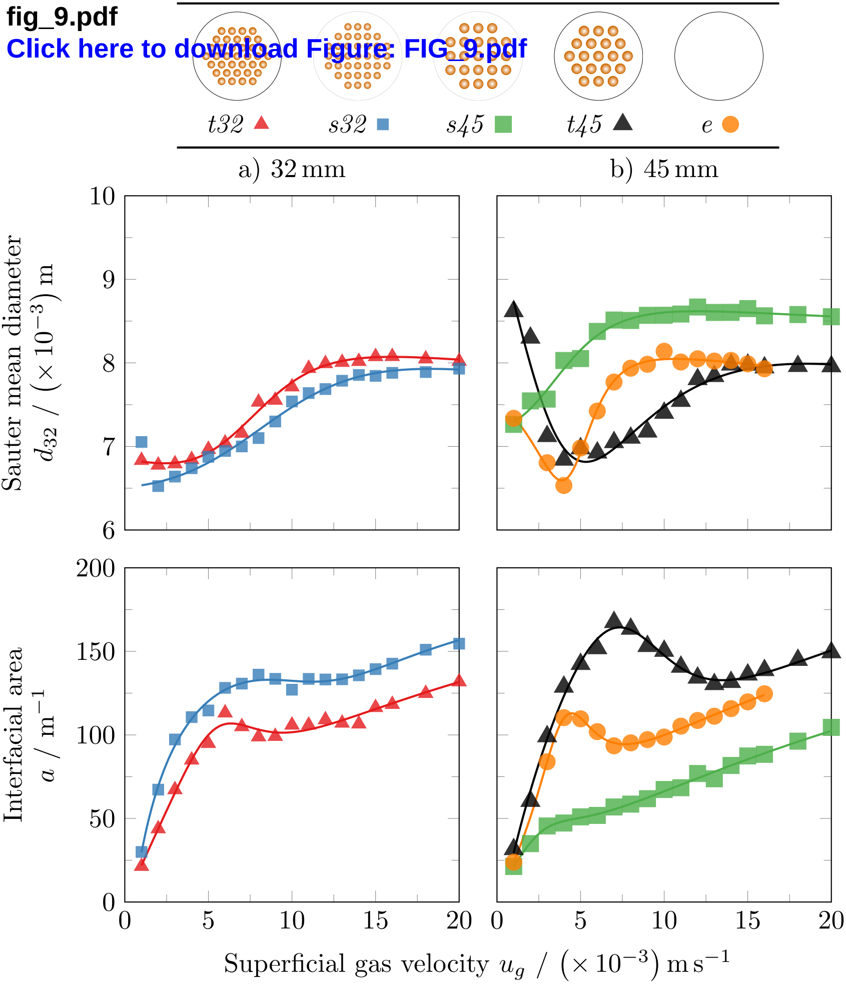

fig_10.pdf
Click here to download Figure: FIG_10.pdf

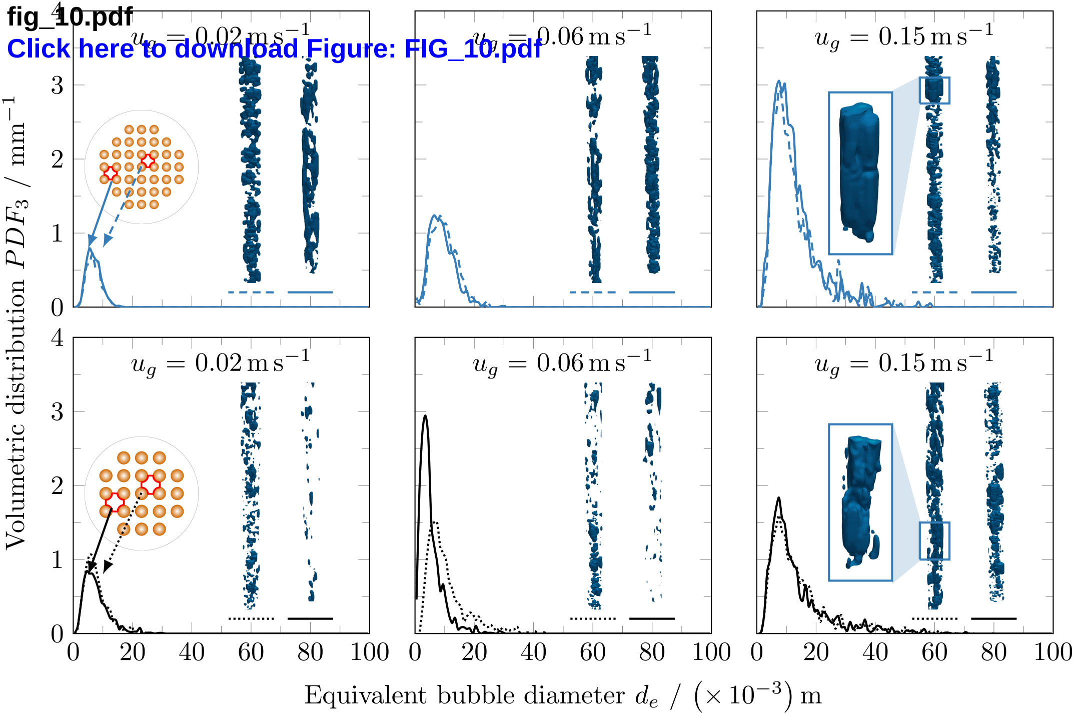

fig_11.pdf
Click here to download Figure: FIG_11.pdf

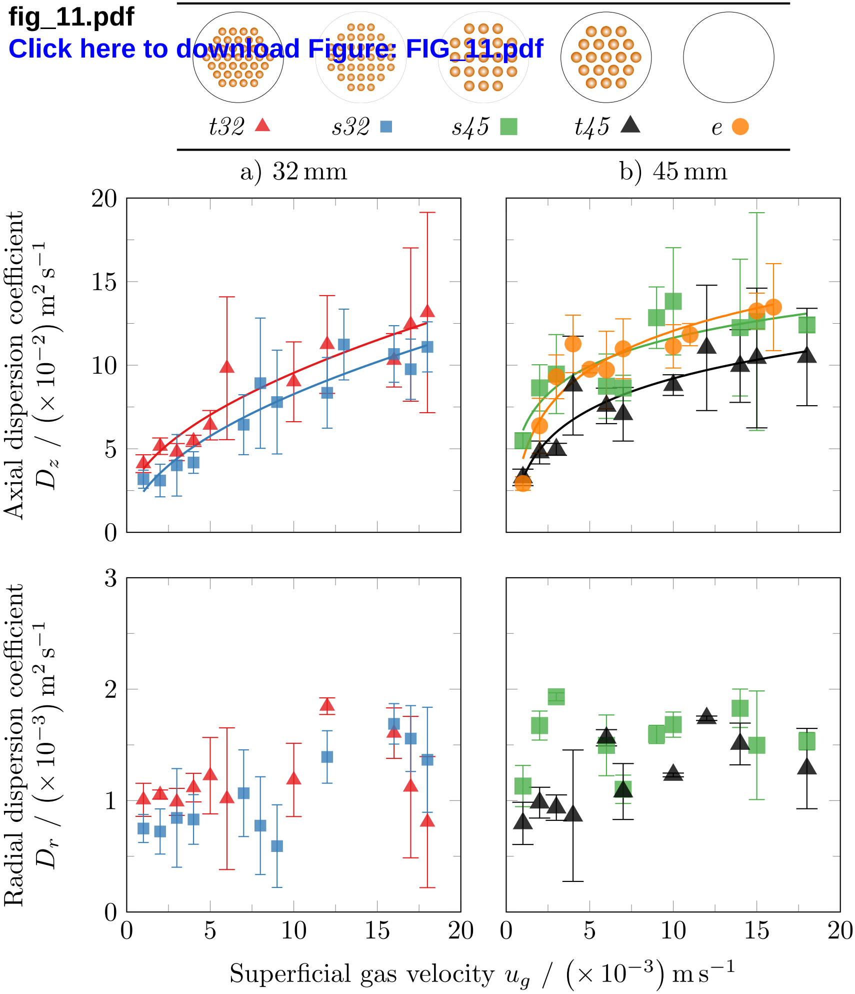

fig_12.pdf
Click here to download Figure: FIG_12.pdf

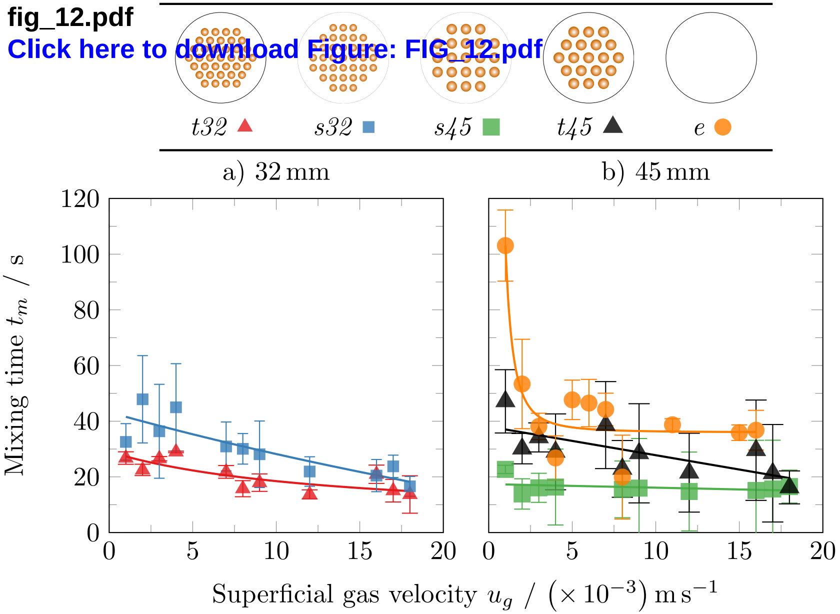

fig_13.pdf
Click here to download Figure: FIG_13.pdf

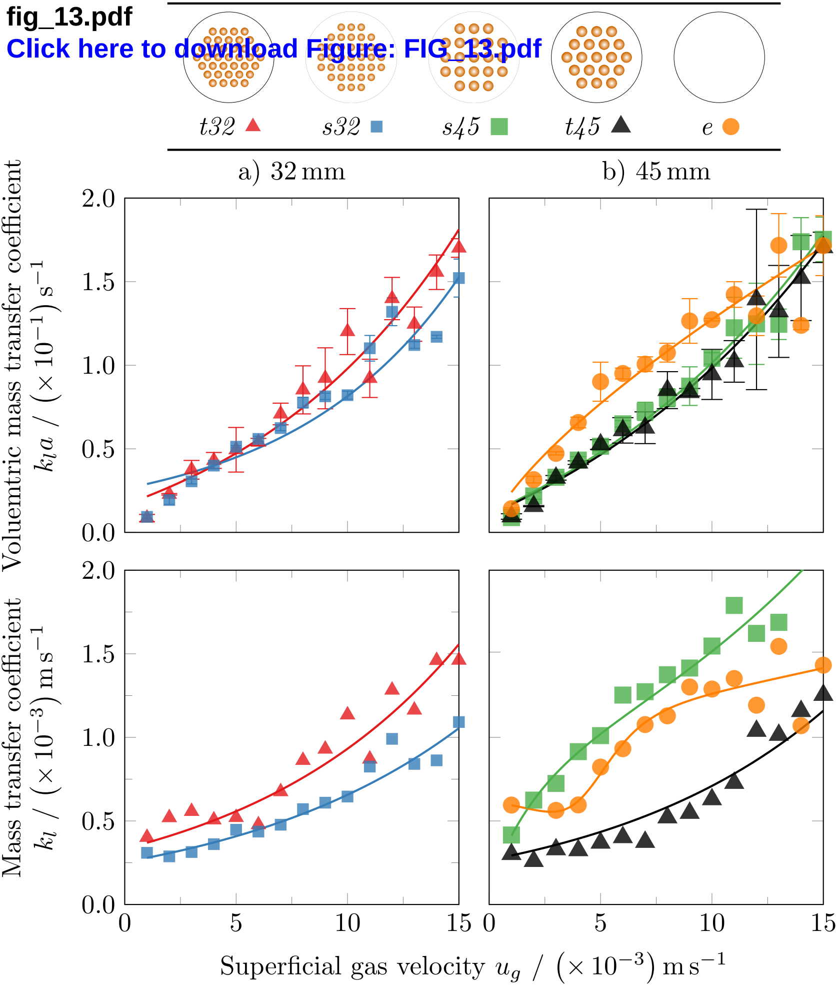

fig_14.pdf
Click here to download Figure: FIG_14.pdf

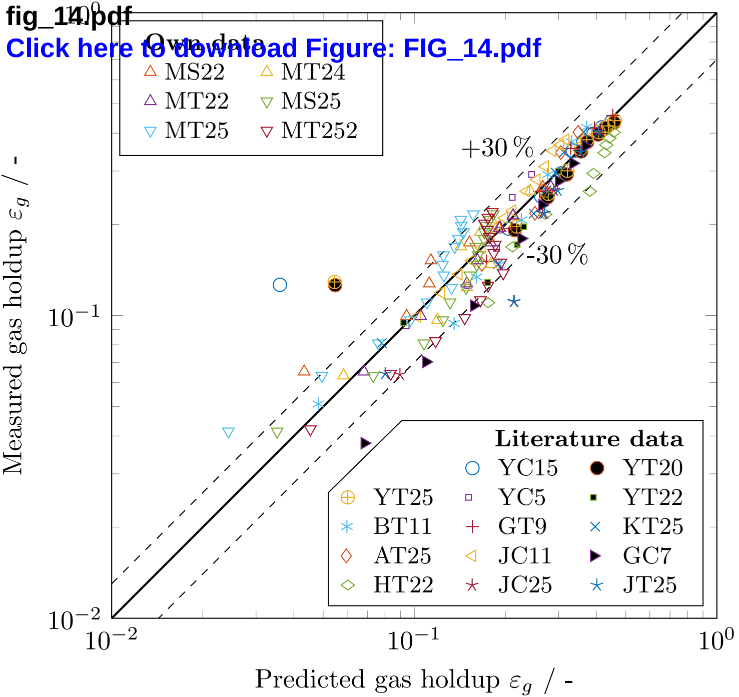

fig_15.pdf
Click here to download Figure: FIG_15.pdf

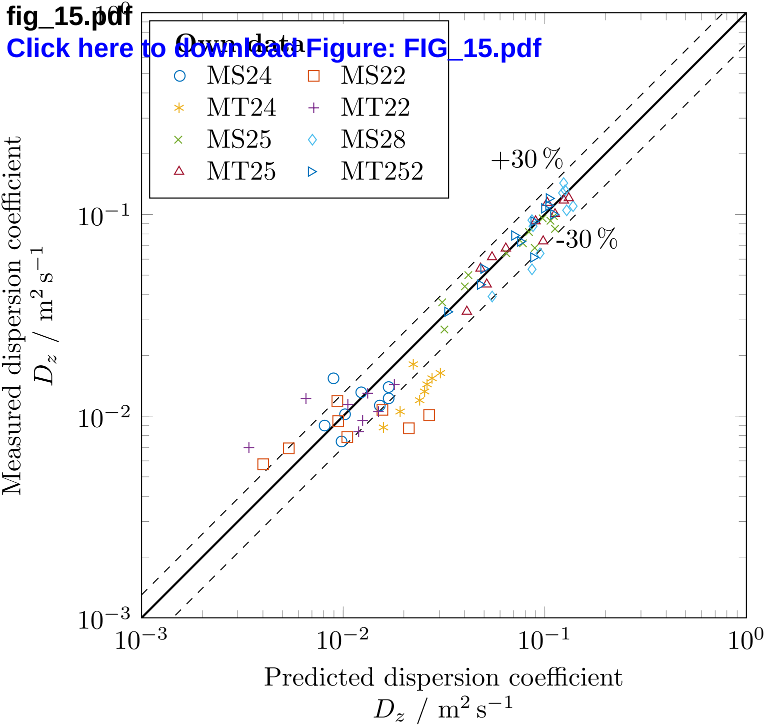

fig_16.pdf
Click here to download Figure: FIG_16.pdf

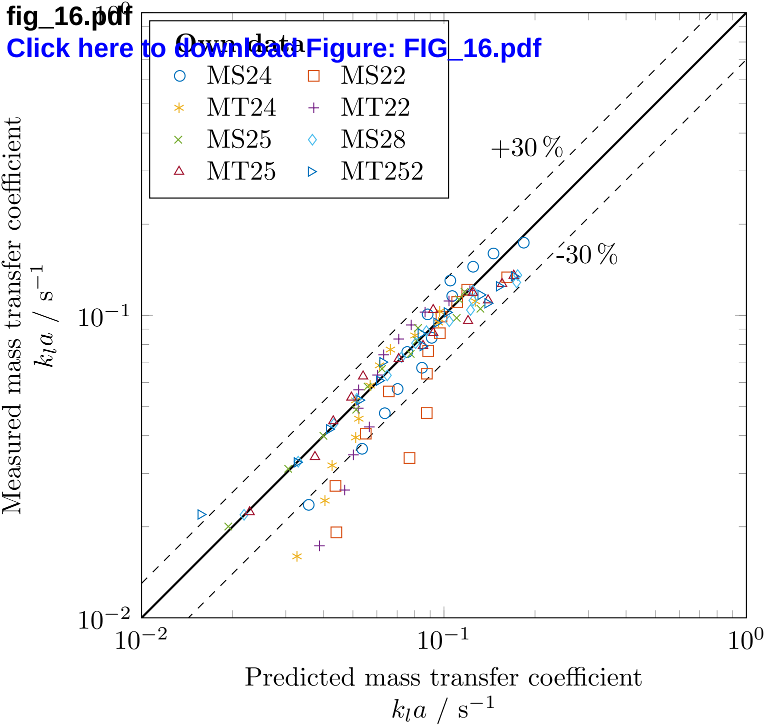

e_2.png

Click here to download high resolution image

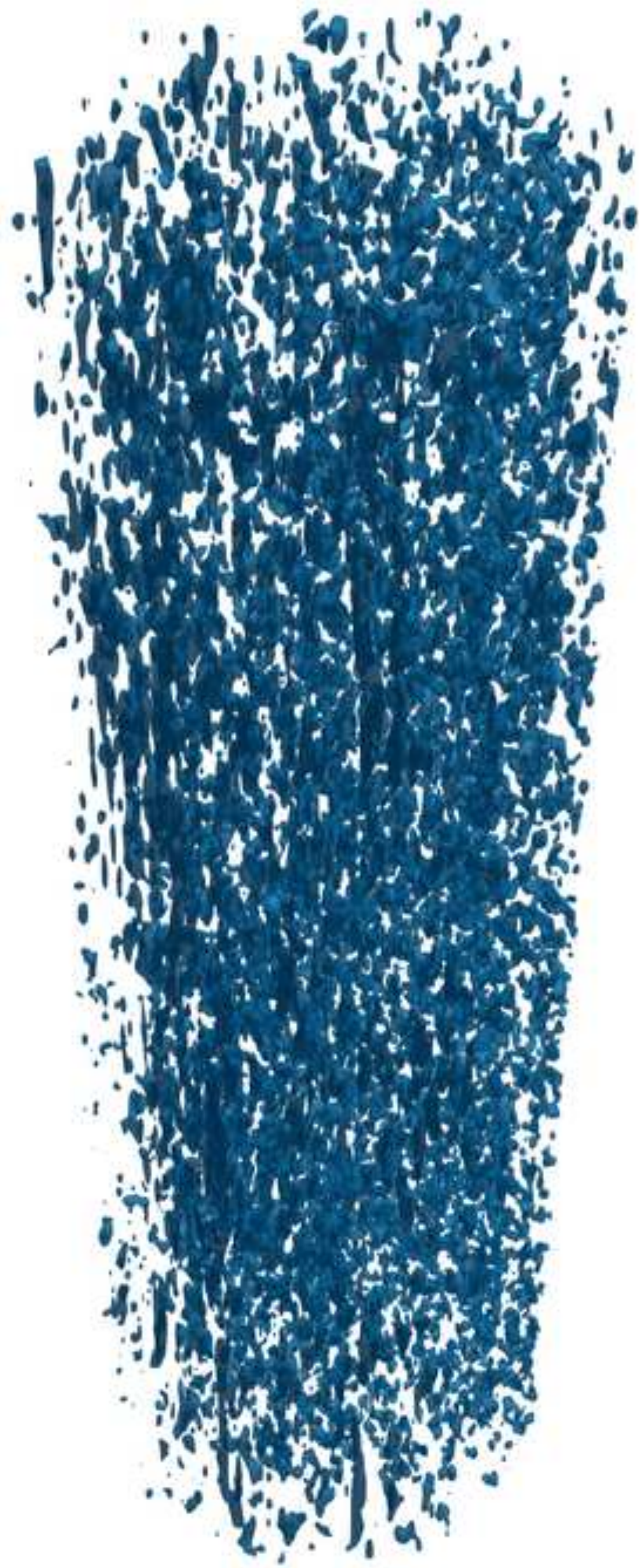

e_6.png

Click here to download high resolution image

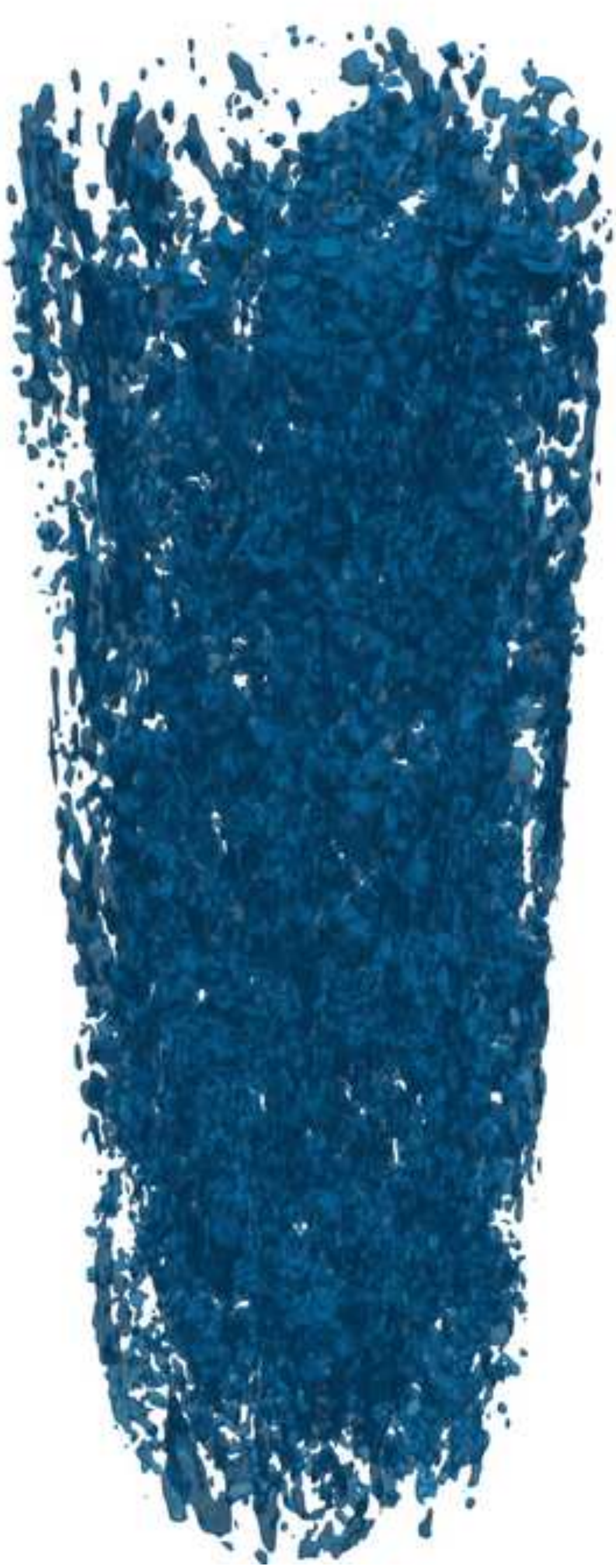

s32_15.png

Click here to download high resolution image

s32_2.png

Click here to download high resolution image

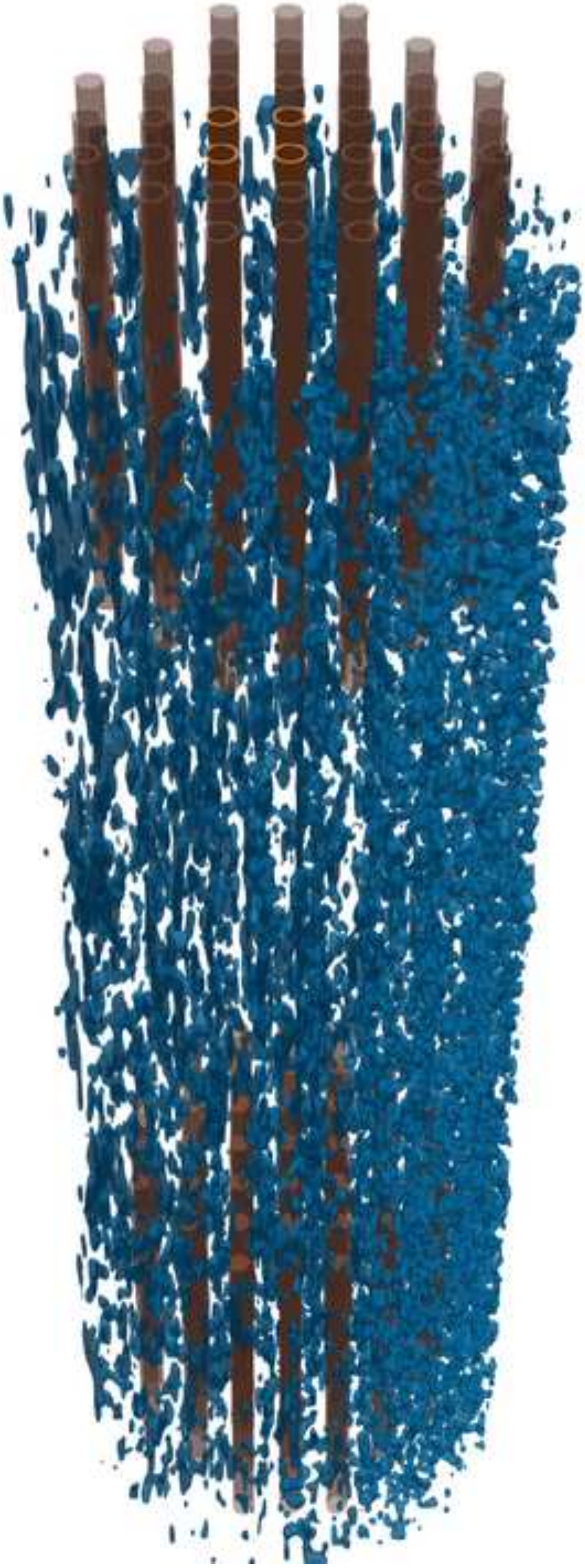

s32_6.png

Click here to download high resolution image

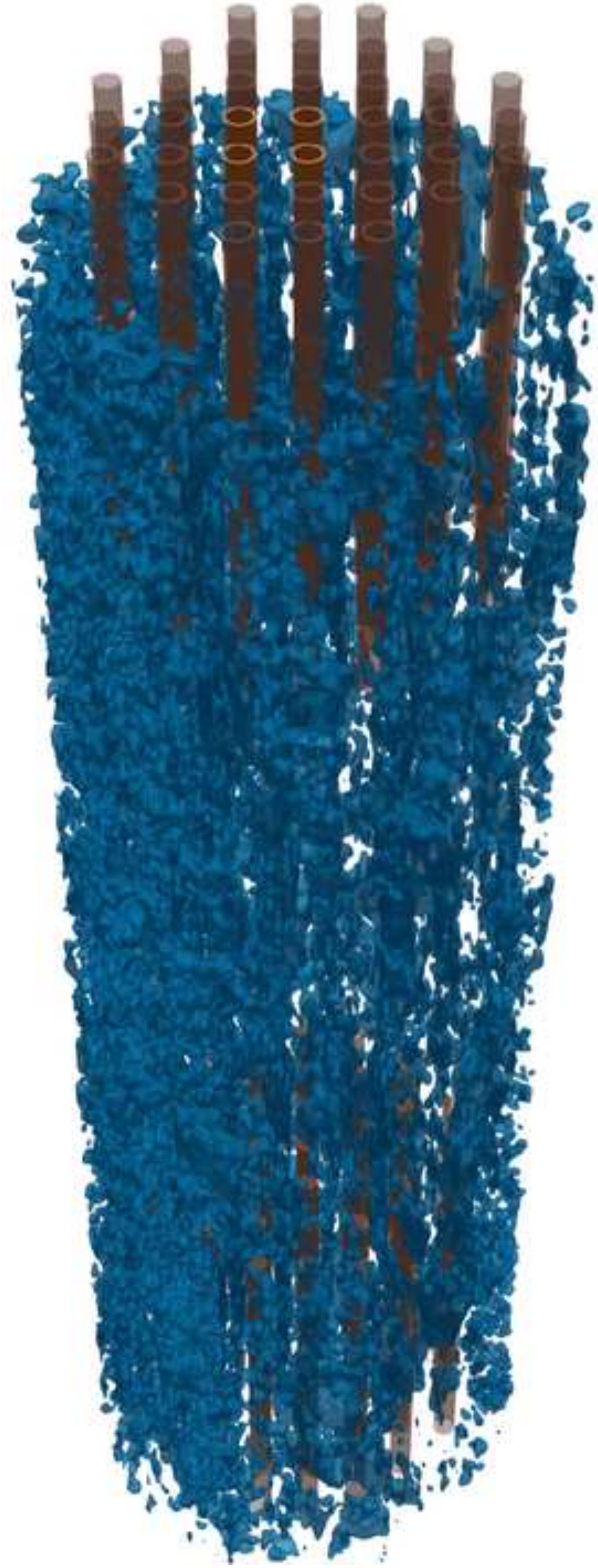

s45_15.png

Click here to download high resolution image

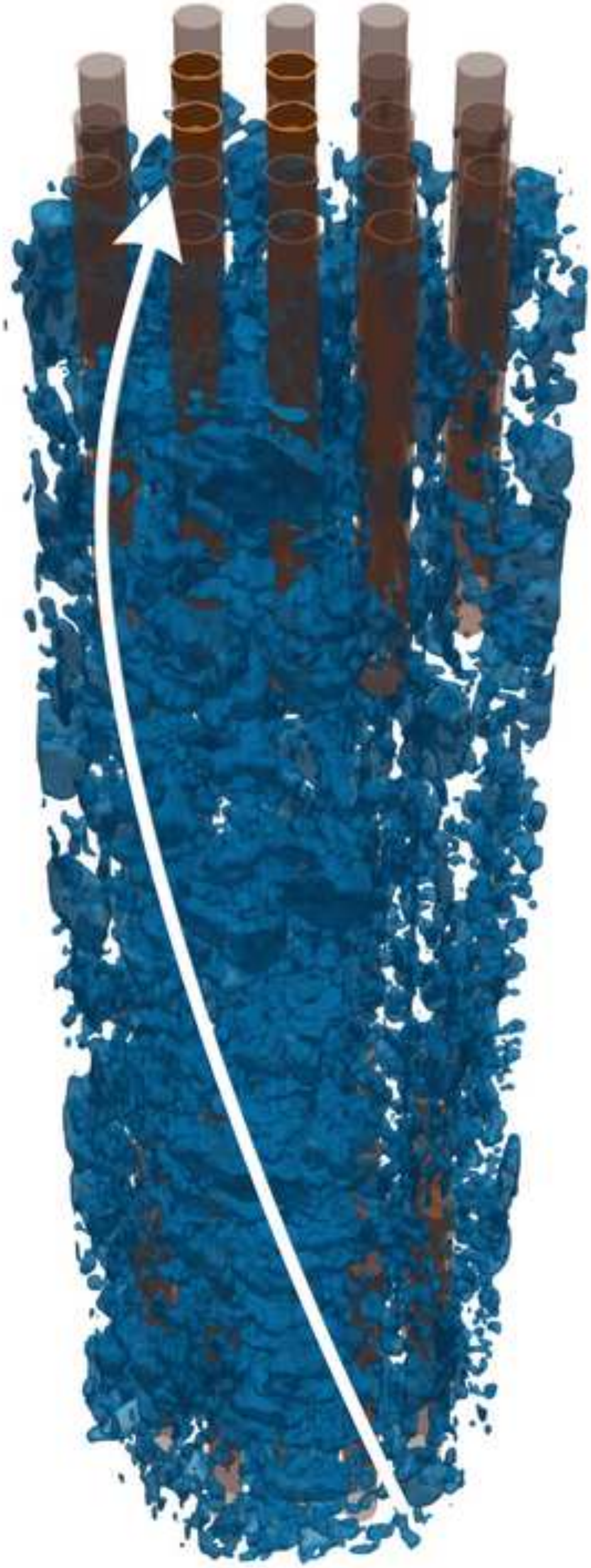

s45_2.png

Click here to download high resolution image

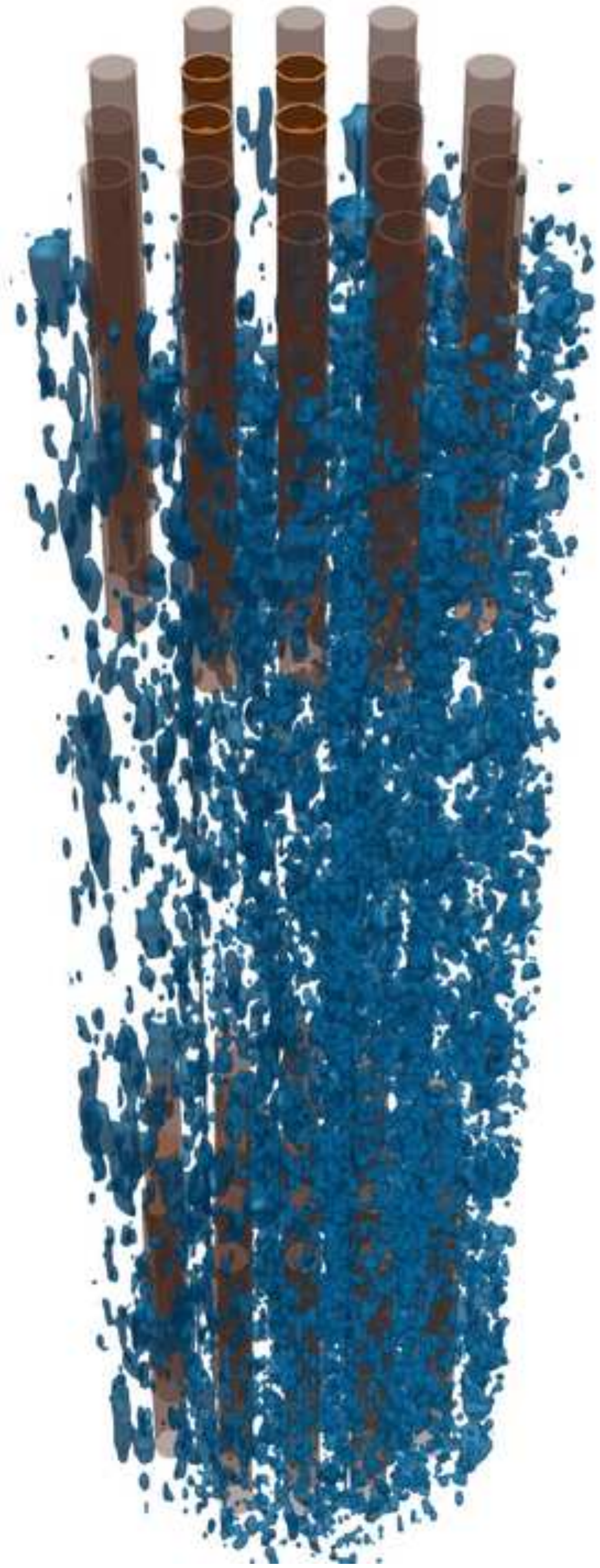

s45_6.png

Click here to download high resolution image

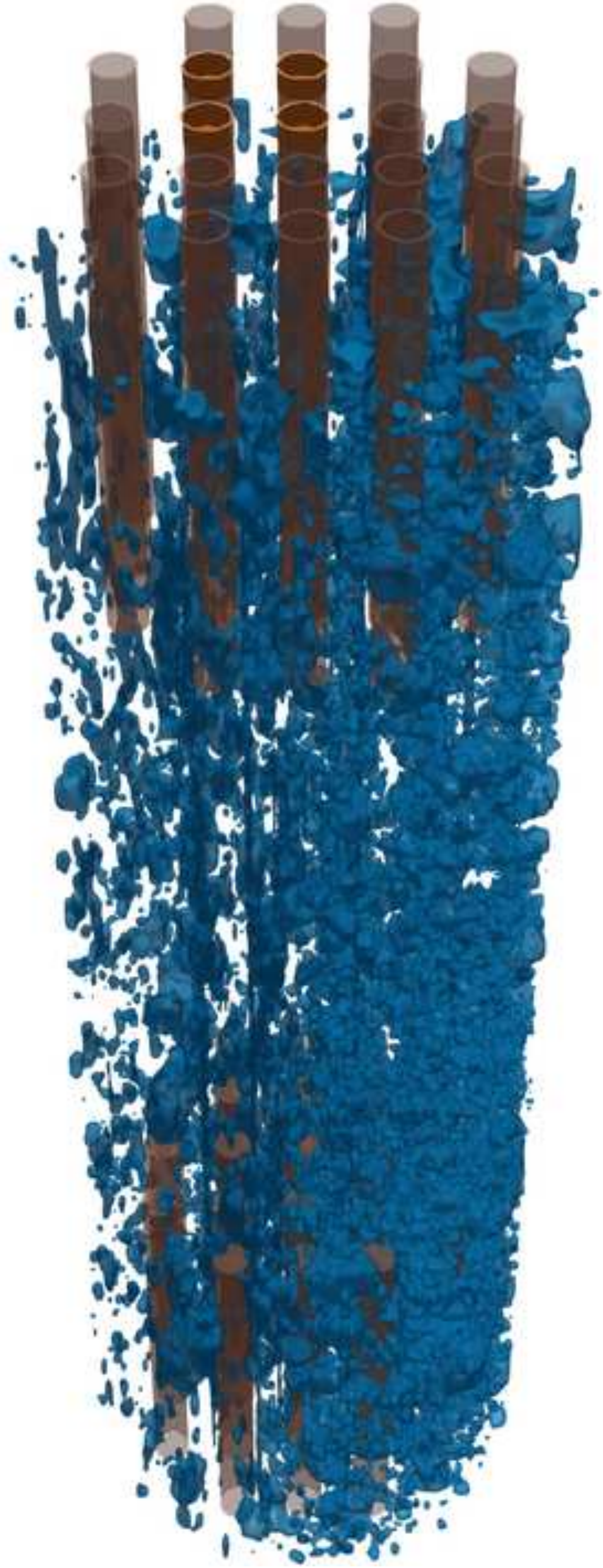

t32_15.png

Click here to download high resolution image

t32_2.png

Click here to download high resolution image

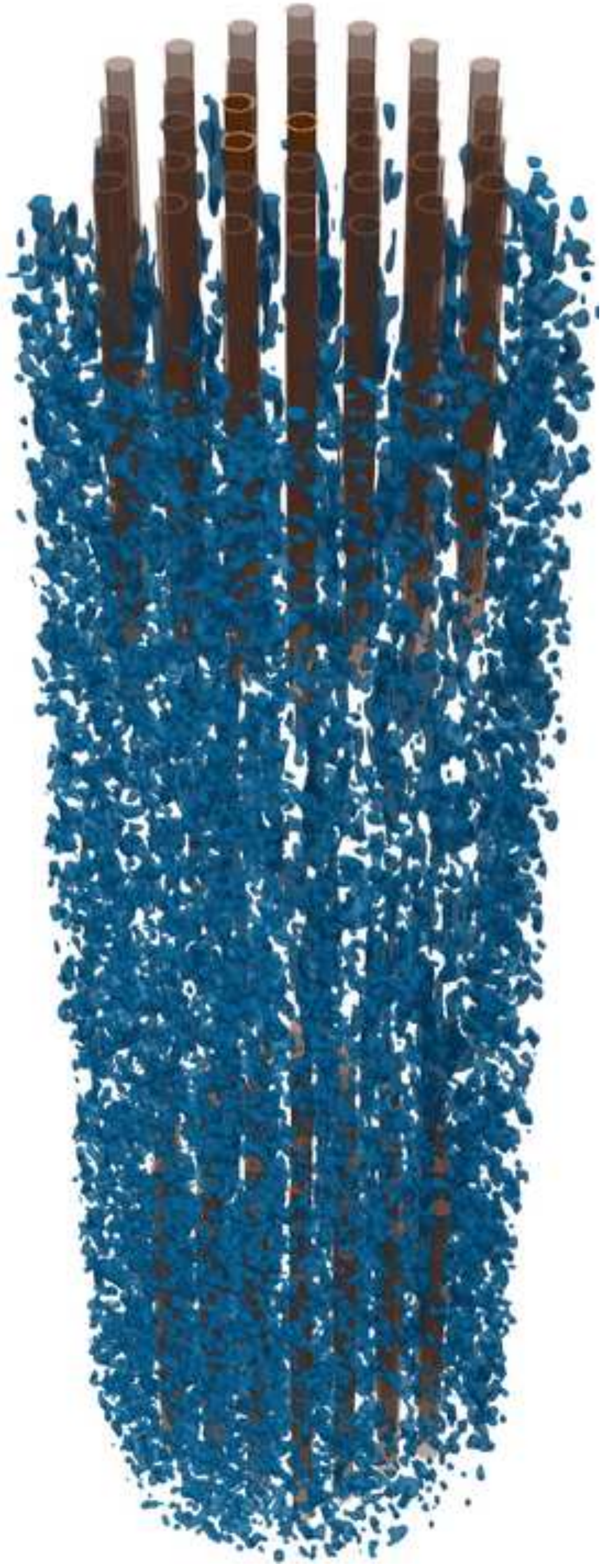

t32_6.png

Click here to download high resolution image

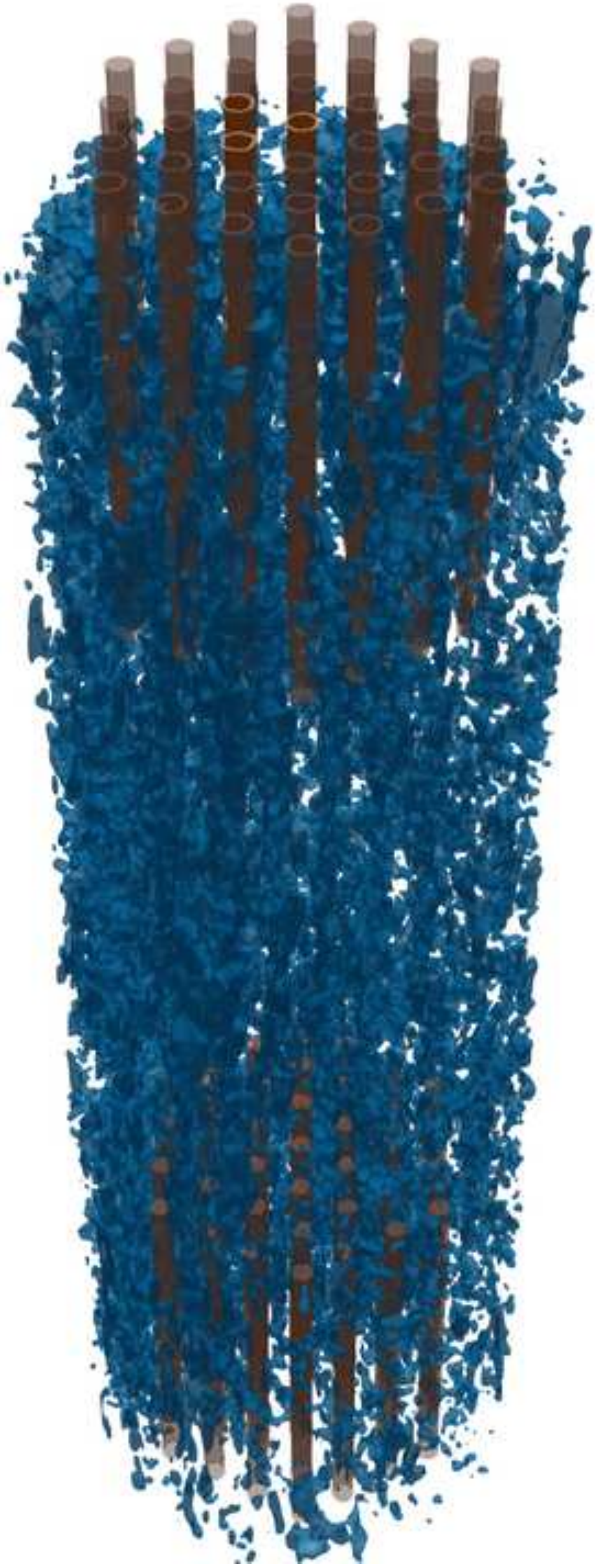

t45_15.png

Click here to download high resolution image

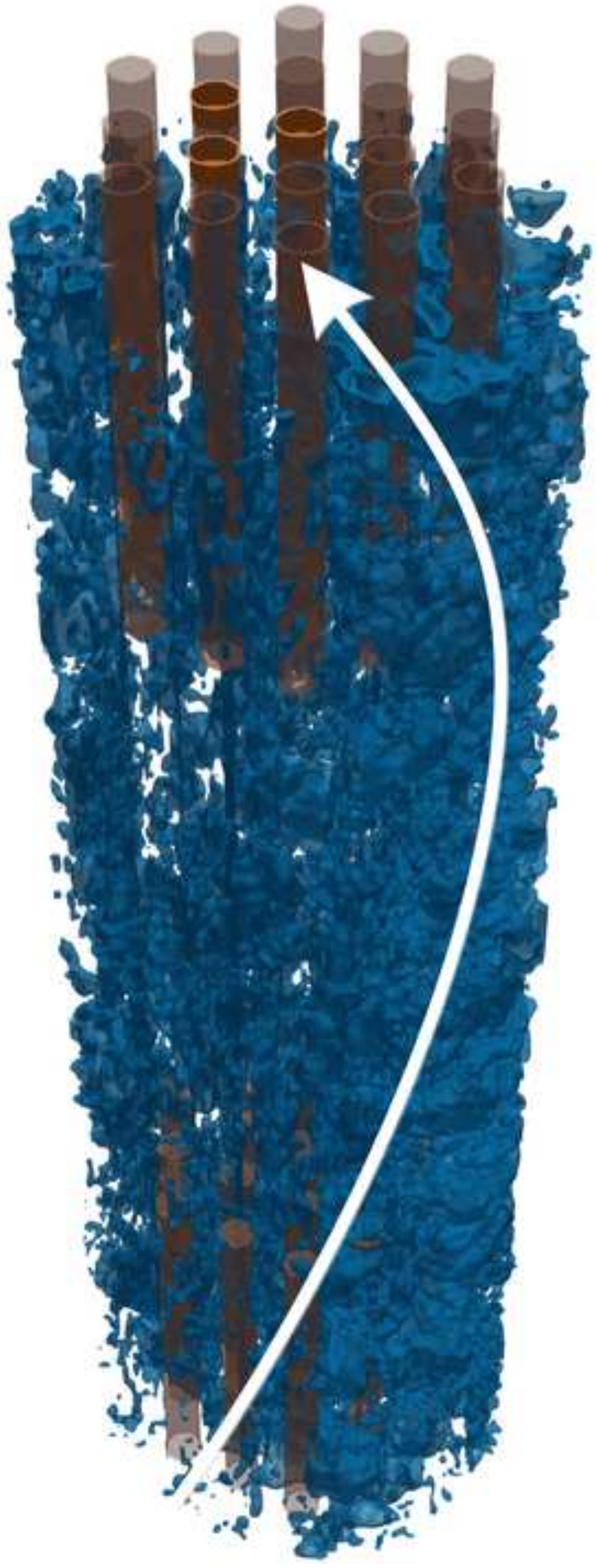

t45_2.png

Click here to download high resolution image

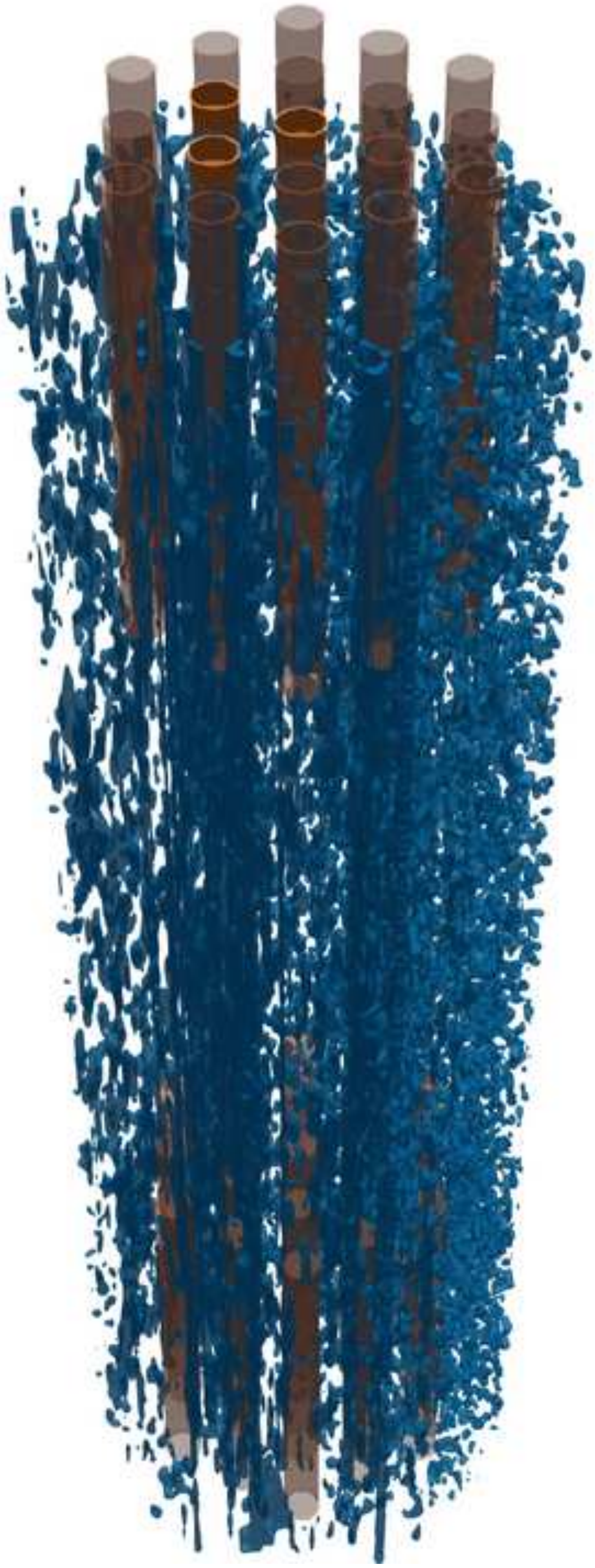

t45_6.png

Click here to download high resolution image

e_15.png

Click here to download high resolution image

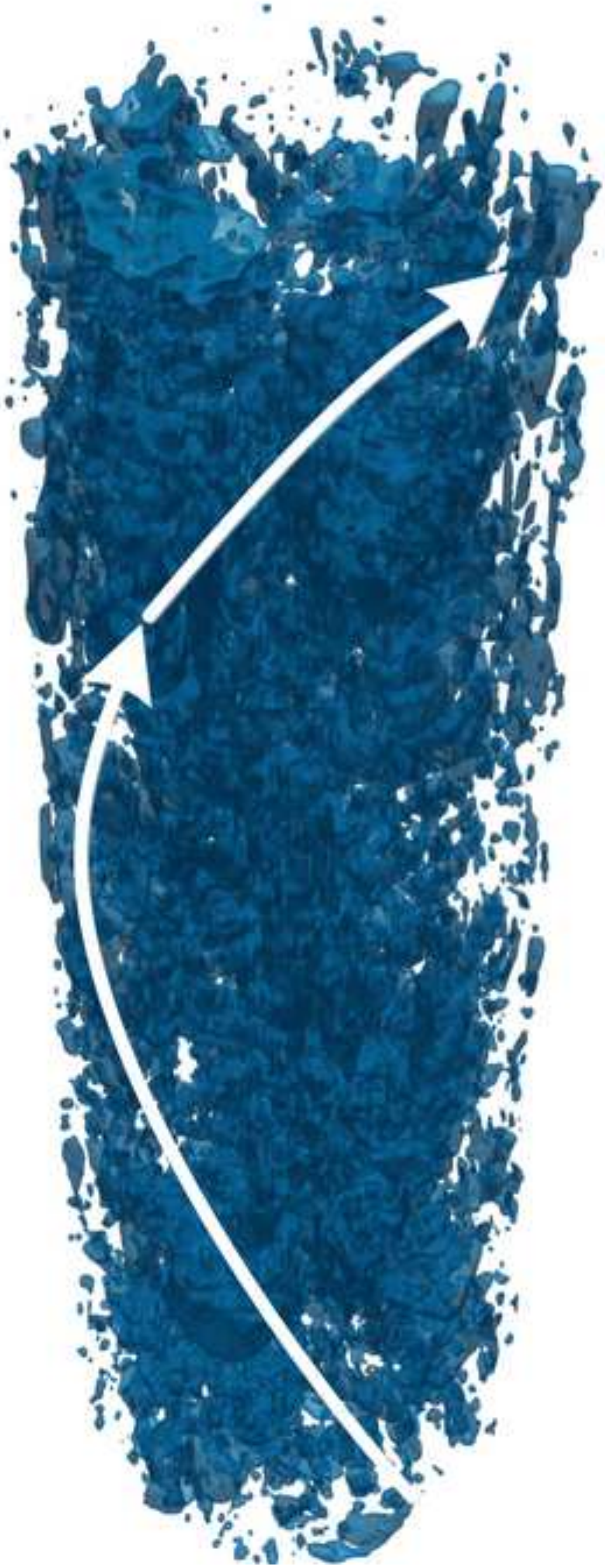

***Declaration of Interest Statement**

Declaration of interests

☒ The authors declare that they have no known competing financial interests or personal relationships that could have appeared to influence the work reported in this paper.

☐The authors declare the following financial interests/personal relationships which may be considered as potential competing interests: